symmetry

MDPI

Article

Photoacoustic Waveform Design for Optimal Parameter Estimation Based on Maximum Mutual Information

Zuwen Sun and Natalie Baddour *

Department of Mechanical Engineering, University of Ottawa, 161 Louis Pasteur, Ottawa, ON K1N 6N5, Canada; zsun046@uottawa.ca

* Correspondence: nbaddour@uottawa.ca

Abstract: Waveform design is a potentially significant approach to improve the performance of an imaging or detection system. Photoacoustic imaging is a rapidly developing field in recent years; however, photoacoustic waveform design has not been extensively investigated. This paper considers the problem of photoacoustic waveform design for parameter estimation under constraints on input energy. The use of information theory is exploited to formulate and solve this optimal waveform design problem. The approach yields the optimal waveform power spectral density. Direct inverse Fourier transform of the optimal waveform frequency spectrum amplitude is proposed to obtain a real waveform in the time domain. Absorbers are assumed to be stochastic absorber ensembles with uncertain duration and location parameters. Simulation results show the relationship between absorber parameter distribution and the characteristics of optimal waveforms. Comparison of optimal waveforms for estimation, optimal waveforms for detection (signal-to-noise ratio) and other commonly used waveforms are also discussed. The symmetry properties of the forward and inverse Fourier Transforms are used to analyze the time and frequency properties and provide a heuristic view of how different goals affect the choice of waveform.

Keywords: waveform engineering; estimation waveform; information theory; photoacoustic imaging; detection waveform

Citation: Sun, Z.; Baddour, N. Photoacoustic Waveform Design for Optimal Parameter Estimation Based on Maximum Mutual Information. *Symmetry* **2024**, *16*, 1402. https://doi.org/10.3390/sym16101402

Academic Editor: Qing-Wen Wang

Received: 19 September 2024
Revised: 8 October 2024
Accepted: 13 October 2024
Published: 21 October 2024

1. Introduction

A photoacoustic imaging (PAI) system designed for biomedical applications offers the combined benefits of optical and acoustical imaging methods. The approach leverages the sensitivity and contrast of optical absorption and minimal scattering in soft tissue of acoustic propagation [1,2]. By using safe, non-ionizing illumination sources, the photoacoustic effect is effectively utilized in biological tissues. Pulsed electromagnetic waves have been the most commonly used excitation source for photoacoustics, as illustrated in the work of Kruger and Wang [3–7]. Notably, in the past decade, continuous wave photoacoustics has attracted attention as it uses less expensive and smaller laser sources [8]. Attempts have been made to improve the photoacoustic system performance, such as improving the signal-to-noise ratio (SNR) [8–10], contrast [11,12], and resolution [13,14], through different methods such as averaging, using contrast agents, and optimizing the input waveforms. Dynamic contrast-enhanced imaging is also drawing extensive attention in photoacoustics in recent years as it provides an additional increase in imaging contrast [15]. Recently, information theory has also been applied in photoacoustic imaging to improve resolution [16] and noise reduction [17].

Waveform design is one of the commonly used methods to improve the performance of imaging or detection modalities. Waveform design involves creating specific signals to optimize performance in applications, yet this topic has not received much attention in photoacoustics. The primary goal of waveform design is to design waveforms that enhance the system's ability to achieve desired tasks under given constraints. In this context, estimation and detection waveforms serve different purposes. Estimation waveforms are

tailored to accurately measure and extract parameters of interest, such as the location or size of a target. They are designed to improve parameter accuracy or precision. In contrast, detection waveforms are optimized to identify the presence or absence of a target or signal. Their design focuses on maximizing the probability of detection, ensuring reliable target identification even in challenging environments. In the well-studied radar modality, optimal waveform design has been developed for optimal detection and optimal parameter estimation problems. In photoacoustics, the problem of designing a waveform for optimal detection has been considered in our previous work [9]. An approach that uses simpler waveforms (Prolate Spheroidal Wave Functions (PSWF) or their discrete relative, Discrete Prolate Spheroidal Sequences (DPSS) was also proposed to achieve near optimal results by exploiting their properties of compactness [10]. However, the problem of optimal waveform design for photoacoustic absorber parameter estimation has yet to be explored.

Bell [18] proposed a method of finding optimal waveforms for estimation in radar applications by leveraging an approach based on information theory. Information theory has mostly been applied to communication technologies [19], specifically to radar since the 1950s [20] and still attracts research attention [21]. However, the applicability of information theory to photoacoustic waveform design has not been addressed in the literature. To date, any attempts at photoacoustic waveform design have been based on deterministic absorber profiles. In this paper, we address the problem of optimal waveform design for photoacoustic absorber parameter estimation. An information theoretic approach is proposed to obtain optimal waveforms for parameter estimation under the assumption of stochastic absorber profiles.

This paper assumes a stochastic absorber ensemble with independent location and duration parameters which follow a Gaussian distribution. The goal of the optimization algorithm is to find the optimal waveform for estimating the parameters of the absorber ensemble with limitations on system bandwidth and input waveform energy. Section 2 formulates the waveform design problem, starting with the photoacoustic wave equation and separating the heating function into absorber absorption profile and laser energy deposition density. Then, information theory is used to obtain the optimal waveform for absorber parameter estimation. Section 3 provides simulations of the proposed approach using numerical methods in MATLAB and discusses the observations on the resulting properties of the optimal waveforms.

Results of this paper show that the optimization algorithm is suitable for photoacoustic imaging systems. The characteristics of the optimal waveforms corresponding to different absorber parameter distributions are discussed. Furthermore, in traditional radar waveform design [18,21], the optimization algorithm only provides the optimal waveform spectrum amplitude in the frequency domain. To obtain a transmittable real waveform in the time domain, we use the direct inverse Fourier transform of the square root of the obtained optimal waveform power spectrum. The time domain waveform obtained from the frequency power spectrum yields in this manner is not unique [22]. However, our proposed approach is a possible approach to finding a real, implementable waveform from the optimal power spectrum. Once the optimal waveform is found by the method in this paper, the numerical method of finding the photoacoustic pressure response and calculating other metrics such as SNR can be found in [9,14]. The laser source that can modulate the laser intensity to the desired optimal temporal profile can be the combination of a fiber laser with an acousto-optic modulator [23].

2. Problem Formulation

2.1. Photoacoustic Imaging

The physics of a photoacoustic system are governed by the photoacoustic equation given by [24]

$$\left(\nabla^2 - \frac{1}{v_s^2}\frac{\partial^2}{\partial t^2}\right) p\left(\vec{r}, t\right) = -\frac{\beta}{C_P}\frac{\partial H\left(\vec{r}, t\right)}{\partial t} \tag{1}$$

where p is the pressure response at position $\vec{r}$ and time t, β is the thermal coefficient of volume expansion, C_p is the heat capacity at constant pressure, and v_s is the speed of sound. $H\left(\vec{r},t\right)$ is the heating function (thermal energy converted per unit volume and per unit time [25]), representing the spatial and temporal distribution of the absorbed optical energy. It is assumed that $H\left(\vec{r},t\right)$ is a separable function of space and time [14], which implies

$$H\left(\vec{r},t\right) = \alpha\left(\vec{r}\right)\phi(t) \tag{2}$$

where $\alpha\left(\vec{r}\right)$ is the absorber absorption coefficient in $\left[\mathrm{cm}^{-1}\right]$ describing the photoacoustic absorber's spatial absorption profile, and $\phi(t)$ is the energy deposition density describing the temporal profile of the laser deposited at the skin (surface), so that

$$E_p = \int_{-\infty}^{\infty} \phi(t)dt \tag{3}$$

is the physical energy deposition per unit area, in $\left[\mathrm{J/cm}^2\right]$. Note that $\phi(t)$ has physical units of $\left[\mathrm{J}/\left(\mathrm{cm}^2 \cdot \mu\mathrm{s}\right)\right]$. In signal processing, the energy of a signal is defined as

$$E = \int_{-\infty}^{\infty} |\phi(t)|^2 dt \tag{4}$$

Considering a 1-D problem in the z direction and substituting $H\left(\vec{r},t\right) = \alpha(z)\phi(t)$ in (1) Gives

$$\left(\frac{\partial^2}{\partial z^2} - \frac{1}{v_s^2}\frac{\partial^2}{\partial t^2}\right)p(z,t) = -\frac{\beta}{C_P}\alpha(z)\frac{\partial\phi(t)}{\partial t} \tag{5}$$

Now applying the temporal Fourier transform gives

$$\frac{\partial^2}{\partial z^2}\widetilde{p}(z,\omega) + \frac{\omega^2}{v_s^2}\widetilde{p}(z,\omega) = -\frac{i\omega\beta}{C_P}\alpha(z)\widetilde{\phi}(\omega) \tag{6}$$

where the tilde $\widetilde{\cdot}$ denotes a temporal Fourier domain and ω is the temporal frequency variable. Then, using the wavenumber $k = \omega/v_s$, we have

$$\frac{d^2}{dz^2}\widetilde{p}(z,\omega) + k^2\widetilde{p}(z,\omega) = -\frac{ikv_s\beta}{C_P}\alpha(z)\widetilde{\phi}(\omega) \tag{7}$$

Taking the spatial Fourier transform of Equation (7), we have

$$\begin{aligned} -{\omega_z}^2\hat{\widetilde{p}}(\omega_z,\omega) + k^2\hat{\widetilde{p}}(\omega_z,\omega) &= -\tfrac{ikv_s\beta}{C_P}\hat{\alpha}(\omega_z)\widetilde{\phi}(\omega) \\ \hat{\widetilde{p}}(\omega_z,\omega) &= -\tfrac{ikv_s\beta}{C_P}\tfrac{\hat{\alpha}(\omega_z)}{(k^2-{\omega_z}^2)}\widetilde{\phi}(\omega) \end{aligned} \tag{8}$$

where the hat $\hat{\cdot}$ denotes a spatial Fourier transform and ω_z is the spatial frequency variable. We make use of the Gruneisen parameter defined as [25]

$$\Gamma = \frac{\beta}{\rho C_V \kappa} \tag{9}$$

where κ is the absorber isothermal compressibility described by

$$\kappa = \frac{C_P}{\rho v_s^2 C_V} \tag{10}$$

where C_v is the heat capacity at constant volume. Note here that C_v and C_p are approximately the same for tissue [25]. Hence, it follows that

$$\Gamma = \frac{\beta}{\rho C_V \frac{C_P}{\rho v_s^2 C_V}} = \frac{v_s^2 \beta}{C_P} \tag{11}$$

Substituting Equation (11) into Equation (8) gives

$$\hat{\tilde{p}}(\omega_z, \omega) = -\frac{ik\Gamma}{v_s} \frac{\hat{\alpha}(\omega_z)}{(k^2 - {\omega_z}^2)} \tilde{\phi}(\omega) \tag{12}$$

Now, we define the absorber transfer function in the (spatial and temporal) Fourier domain as

$$\hat{\tilde{\theta}}(\omega_z, k) = \frac{ik\Gamma}{v_s} \frac{\hat{\alpha}(\omega_z)}{({\omega_z}^2 - k^2)} \tag{13}$$

It then follows that

$$\hat{\tilde{p}}(\omega_z, \omega) = \hat{\tilde{\theta}}(\omega_z, k) \tilde{\phi}(\omega) \tag{14}$$

Equation (14) clearly demonstrates the input/output relationship between the input $\phi(t)$ energy deposition density, the absorber transfer function $\hat{\tilde{\theta}}(\omega_z, k)$ and the output pressure response $\hat{\tilde{p}}(\omega_z, \omega)$.

Taking the inverse spatial Fourier transform of (13) gives

$$\tilde{\theta}(z, k) = \frac{1}{2\pi} \int_{-\infty}^{\infty} \hat{\tilde{\theta}}(\omega_z, k) e^{i\omega_z z} d\omega_z = \frac{ik\Gamma}{v_s} \frac{1}{2\pi} \int_{-\infty}^{\infty} \frac{\hat{\alpha}(\omega_z)}{({\omega_z}^2 - k^2)} e^{i\omega_z z} d\omega_z \tag{15}$$

Using the standing wave case in Theorem 5 of [26], and assuming $\hat{\alpha}(\omega_z)$ has no poles and remains bounded, we have

$$\frac{1}{2\pi} \int_{-\infty}^{\infty} \frac{\hat{\alpha}(\omega_z)}{({\omega_z}^2 - k^2)} e^{i\omega_z z} d\omega_z = \begin{cases} \frac{1}{2ik} \hat{\alpha}(-k) e^{-ikz} & z > 0 \\ \frac{1}{2ik} \hat{\alpha}(k) e^{ikz} & z < 0 \end{cases} \tag{16}$$

Hence, Equation (15) becomes

$$\tilde{\theta}(z, k) = \frac{\Gamma}{2v_s} \begin{cases} \hat{\alpha}(-k) e^{-ikz} & z > 0 \\ \hat{\alpha}(k) e^{ikz} & z < 0 \end{cases} \tag{17}$$

The system impulse response in the time domain is found by taking the inverse temporal Fourier transform of the transfer function

$$\begin{aligned} \theta(z, t) &= \frac{1}{2\pi} \int_{-\infty}^{\infty} \tilde{\theta}(z, k) e^{i\omega t} d\omega \\ &= \frac{\Gamma}{4\pi v_s} \begin{cases} \int_{-\infty}^{\infty} \hat{\alpha}\left(-\frac{\omega}{v_s}\right) e^{-i\omega \frac{z}{v_s}} e^{i\omega t} d\omega & z > 0 \\ \int_{-\infty}^{\infty} \hat{\alpha}\left(\frac{\omega}{v_s}\right) e^{i\omega \frac{z}{v_s}} e^{i\omega t} d\omega & z < 0 \end{cases} \end{aligned} \tag{18}$$

Solving Equation (18) gives the absorber impulse response as

$$\theta(z, t) = \frac{\Gamma}{2} \begin{cases} \alpha(z - v_s t) & z > 0 \\ \alpha(z + v_s t) & z < 0 \end{cases} \tag{19}$$

Equation (19) shows that the impulse response of the absorber has exactly the same spatial shape of the inhomogeneity (absorber), although it is a function in time whereas the shape of the absorber is a function of space. The speed of sound in the medium is the converting factor that relates distances in space to durations in time. The expression for photoacoustic imaging in input/output form is then given by

$$p(z,t) = \theta(z,t) * \phi(t) \tag{20}$$

where $*$ denotes convolution.

2.2. Optimal Estimation Waveform Design Problem

Viewing the photoacoustic imaging system in an input/output form, for detection at some fixed location z, we have the block diagram shown in Figure 1.

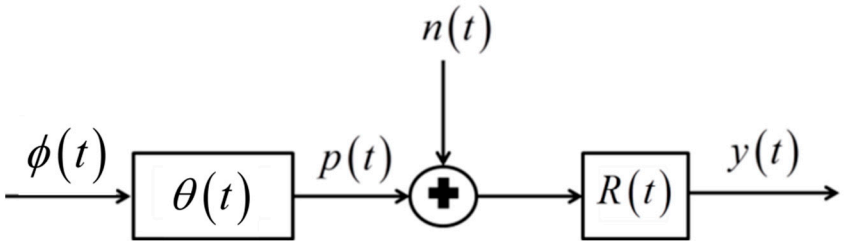

Figure 1. Block diagram of photoacoustic imaging (detection at a fixed location).

At a fixed detection location z, the pressure response signal $p(t)$ is received at the receiver filter $R(t)$ in the presence of additive noise process $n(t)$. The noise is assumed to be stationary and ergodic, and to have power spectral density (PSD) $P_{nn}(f)$. Furthermore, the noise is assumed to be statistically independent of both the energy deposition density $\phi(t)$ and the absorber impulse response $\theta(t)$.

We now examine some properties of an absorber impulse response ensemble $\Theta(t)$ with N absorbers and with probability measures assigned to each $\theta_i(t)$, $i = 1..N$. We assume the back propagation case ($z < 0$) in Equation (17), and we assume monotone laser radiation as in most PAI systems [14,27,28], where the laser reacts with a single type of absorber such as hemoglobin. We also assume that the absorber ensemble can be modeled as a collection of randomly distributed absorbers [29]. It then follows that.

$$\widetilde{\theta}_i(z_i,k) = \frac{\Gamma}{2v_s}\hat{\alpha}_i(k)e^{ikz_i} \tag{21}$$

where z_i (a negative number) denotes the distance between the transducer and the i^{th} absorber.

In the time domain, then

$$\theta_i(z_i,t) = \frac{\Gamma}{2}\alpha_i(z_i + v_s t) \tag{22}$$

From Equation (20) and using the notation $\omega = 2\pi f$, we have

$$|\widetilde{p}(f)|^2 = \left|\widetilde{\theta}(f)\right|^2 |\widetilde{\phi}(f)|^2 \tag{23}$$

Taking the expectation with respect to the ensemble $\widetilde{\Theta}(f)$, the mean-square spectrum of $p(t)$ is

$$\mathrm{E}|\widetilde{p}(f)|^2 = E\left\{\left|\widetilde{\Theta}(f)\right|^2\right\}|\widetilde{\phi}(f)|^2 \tag{24}$$

Now, the expectation with respect to the ensemble can be written as [18]

$$\mathrm{E}\left|\widetilde{\Theta}(f)\right|^2 = |\mu_\theta(f)|^2 + \sigma_\theta^2(f) \tag{25}$$

where $\mu_\theta(f)$ is the mean of $\widetilde{\Theta}(f)$,

$$\mu_\theta(f) = \mathrm{E}\left\{\widetilde{\Theta}(f)\right\} \tag{26}$$

and $\sigma_\theta^2(f)$ is the variance of $\widetilde{\Theta}(f)$,

$$\sigma_\theta^2(f) = \mathrm{E}\left\{\left|\widetilde{\theta}(f) - \mu_\theta(f)\right|^2\right\} \tag{27}$$

We are interested primarily in $\sigma_\theta^2(f)$ for the absorber ensemble, as the pressure signal $p(t)$ corresponding to the mean $\mu_\theta(f)$ is known for a known $\widetilde{\phi}(f)$. It thus provides no information about the absorber. Similarly, we have

$$\mathrm{E}|\widetilde{p}(f)|^2 = |\mu_p(f)|^2 + \sigma_p^2(f) \tag{28}$$

where $\mu_p(f)$ is the mean of $\widetilde{p}(f)$, and $\sigma_p^2(f)$ is the variance of $\widetilde{p}(f)$.

Now considering the photoacoustic measurement system shown in Figure 1, we have a random absorber $\theta(t)$ that consists of parameters that characterize the absorber we wish to measure, and a probabilistic model of the unknown parameters that is meaningful (modeled by the probability distribution of absorber ensemble $\Theta(t)$). The measurement system maps $\theta(t)$ into the random vector $y(t)$. The observer observes $y(t)$ and then determines the desired description of $\theta(t)$. The measurement mechanism is assumed to have inherent inaccuracies, so its measurements contain errors. This can be modeled by assuming that the measurement mechanism stochastically maps the random vector $\theta(t)$ to the random vector $y(t)$. We will denote the mutual information between $\theta(t)$ and $y(t)$ to $I(\theta(t); y(t))$. The mutual information $I(\theta(t); y(t))$ tells us the quantity of information that the observation of $y(t)$ provides about $\theta(t)$. In other words, $I(\theta(t); y(t))$ is the amount of information that the measurement $y(t)$ provides about the absorber parameter vector $\theta(t)$.

Hence, the problem of interest can now be stated as follows. Given a random absorber ensemble $\Theta(t)$ having spectral variance $\sigma_\theta^2(f)$, find the waveforms $\phi(t)$ that maximize the mutual information $MI(\Theta(t); y(t)|\phi(t))$ between the absorber ensemble impulse response and the received waveform, $y(t)$. The spectral variance $\sigma_\theta^2(f)$ is the variance of the absorbers' transfer functions $\widetilde{\theta}(f)$ at all frequencies, calculated via Equation (27). The mutual information is a function of the deterministic input waveform $\phi(t)$, and we are interested in finding the functions $\phi(t)$ that maximize $MI(\Theta(t); y(t)|\phi(t))$ under constraints on energy and bandwidth of the input waveform $\phi(t)$.

Consider an ideal bandpass receiver filter with bandwidth $[-W, W]$ (W can also denote PAI system frequency limitations), and an observation time interval T_O. The observation time interval T_O must be long enough to capture all but a negligible portion of the pressure response $p(t)$, i.e., T_O must be larger than the sum of the characteristic duration of the input waveform $2T$ and the absorber characteristic duration T_a (size of the absorber converted into a duration via the speed of sound). Here, we are assuming that the input waveform is nonzero only between $[-T, T]$, and hence has duration $2T$. It should be noted that in radar applications the target impulse response duration is much shorter than the input waveform duration, hence T_O is usually assumed to be equal to the duration of the input waveform ($2T$) [18].

The problem can now be stated as follows. Given a target ensemble $\widetilde{\Theta}(f)$ of N absorbers with random impulse responses $\widetilde{\theta}_i(f), i = 1..N$, find the $[-T, T]$ time limited and $[-W, W]$ band concentrated optical energy deposition density waveforms $\phi(t)$ with limited energy that maximize the mutual information between the output waveform

and the absorber ensemble impulse response $MI(\Theta(t); y(t)|\phi(t))$. From [18], the mutual information is given by

$$MI(\Theta(t); y(t)|\phi(t)) = T_O \int_{-W}^{W} \ln\left[1 + \frac{2|\phi(f)|^2 \sigma_\Theta^2(f)}{P_{nn}(f) T_O}\right] df \tag{29}$$

To address this problem, we start by defining

$$M(f) = \frac{P_{nn}(f) T_O}{2\sigma_\theta^2(f)} \tag{30}$$

and the total energy of the optical energy deposition density given by

$$\int_{-W}^{W} \left|\widetilde{\phi}(f)\right|^2 df = E \tag{31}$$

Then the $\left|\widetilde{\phi}(f)\right|^2$ that maximizes $MI(\Theta(t); y(t)|\phi(t))$ under the energy constraint is given by

$$\left|\widetilde{\phi}(f)\right|^2 = \max[0, A - M(f)] \tag{32}$$

where the constant A is determined by solving the following equation

$$E = \int_{-W}^{W} \max[0, A - M(f)] df \tag{33}$$

Substituting the expression

$$\left|\widetilde{\phi}(f)\right|^2 = A - M(f) \tag{34}$$

into the energy constraint (27), we have

$$A = \frac{E}{2W} + \frac{1}{2W} \int_{-W}^{W} \frac{P_{nn}(f) T_O}{2\sigma_\theta^2(f)} df \tag{35}$$

However, the direct use of (35) would result in an invalid $\left|\widetilde{\phi}(f)\right|^2$ with negative values. Hence, we must first solve for values of A that satisfy (33) numerically. An easy way of solving $\left|\widetilde{\phi}(f)\right|^2$ can be by first using $A = \min[M(f)]$ and then finding the energy E using (33). If E is not the same (allowable numerical error should be accepted) as the energy constraint, then increase A by a small step and calculate E again. This process is repeated until E is the same as the constraint, within acceptable numerical error.

In this manner, the optimal waveform power spectrum in the frequency domain $\left|\widetilde{\phi}(f)\right|^2$ is found. This approach yields the optimal waveform power spectrum, for which there are multiple possible corresponding waveforms in the time domain. That is, there is no unique solution to obtain the optimal waveform $\phi(t)$ in the time domain given only the power spectrum $\left|\widetilde{\phi}(f)\right|^2$ [22]. There are many methods on recovering a signal in the time domain from its magnitude spectrum in the frequency [22,30–32]. However, all these approaches need some additional assumption on either phase information or some portion of the original signal in the time domain. The optimal waveform in time does not need to be unique, i.e., any waveform that gives the corresponding power spectrum $\left|\widetilde{\phi}(f)\right|^2$ will be optimal. Hence, in this paper we use the direct inverse Fourier transform of the

square root of $\left|\widetilde{\phi}(f)\right|^2$ to obtain one (of many possible) applicable optimal waveform in the time domain.

2.3. Noise Levels and Safety Standards in Photoacoustic

The noise level $N_a(f)$, in units of $[J{\cdot}s]$ in a photoacoustic system mainly comes from thermal acoustic noise [33], which can be described via

$$N_a(f) = \eta(f) k_B Temp \tag{36}$$

where $\eta(f)$ is the detector efficiency at frequency f, k_B is the Boltzmann constant, and $Temp$ is the absolute temperature of the medium. The typical noise level for a photoacoustic system is approximately $40[\mu V]$, which is $6.7[\text{Pa}] = 6.7\left[\text{J/m}^3\right] = 6.7 \times 10^{-6}\left[\text{J/cm}^3\right]$ [34]. Here, it is assumed that the noise is white in frequency and has its total energy concentrated in the frequency range $[-W, W]$, hence the noise spectrum is $P_{nn}(f) = \frac{E_n}{2W}$ where E_n is the noise level in units of $\left[\text{J/cm}^3\right]$.

The safety standard [35] sets the maximum exposure (MPE) level for 1064 nm laser with duration T on human skin as

$$E_{MPE} = 5.5T^{0.25}\left[\text{J/cm}^2\right] \tag{37}$$

2.4. Absorber Ensemble Modelling

Absorbers in this paper are considered to be thin layer (1D) absorbers with thickness l, located at a distance d from the receiver. We assume that there is no decay of the laser inside the absorber. The absorber can be modeled as

$$\theta(t) = \frac{\Gamma}{2}\begin{cases} 1, & \frac{d}{v_s} \le t \le \frac{d+l}{v_s} \\ 0, & Otherwise \end{cases} \tag{38}$$

Defining

$$t_0 = \frac{d}{v_s} \tag{39}$$

as the location of absorber, and

$$T_a = \frac{l}{v_s} \tag{40}$$

as the duration (size) of the absorber, then it follows that

$$\theta(t) = \frac{\Gamma}{2}\begin{cases} 1, & t_0 \le t \le t_0 + T_a \\ 0, & Otherwise \end{cases} \tag{41}$$

Typical values of the Gruneisen parameter Γ for blood are 0.152~0.226 [36]. More detailed information for blood and other types of absorbers such as fat, lipid, and Serum can be found in [37]. We refer to this absorber as the 'square absorber' since the temporal profile from Equation (41) resembles that of a square wave. The simulations in this paper use $\Gamma = 0.2$, with varying location and duration of absorbers to form the absorber ensemble.

3. Simulations

This section shows some examples of finding optimal waveforms for the laser energy deposition density and gives guidelines for how to choose the laser waveform for different absorber ensemble profiles. Simulations are performed with Matlab R2019b. Random parameters of the absorbers are generated through random number generator *normrnd*, which requires the Statistics and Machine Learning Toolbox.

3.1. Example of Absorber Ensemble with Unknown Thickness

The first ensemble consists of an ensemble of absorbers of known location but unknown size (thickness). We consider an absorber ensemble consisting of 100 square absorbers with the same known location $t_0 = \frac{z}{v_s} = 5[\mu s]$ (i.e., distance from receiver z in Equation (19) is 7.5[mm] and speed of sound v_s is 1500[m/s]). The durations (size) of the absorbers T_a (absorber thickness divided by speed of sound) are unknown and follow a Gaussian distribution with mean duration of $\mu_{T_a} = 5[\mu s]$ (that is, the mean thickness is 7.5[mm] and the distribution of thicknesses follow a Gaussian distribution around that mean) and standard deviation $\sigma = 2[\mu s]$. The distribution of duration and location parameters is shown in Figure 2a.

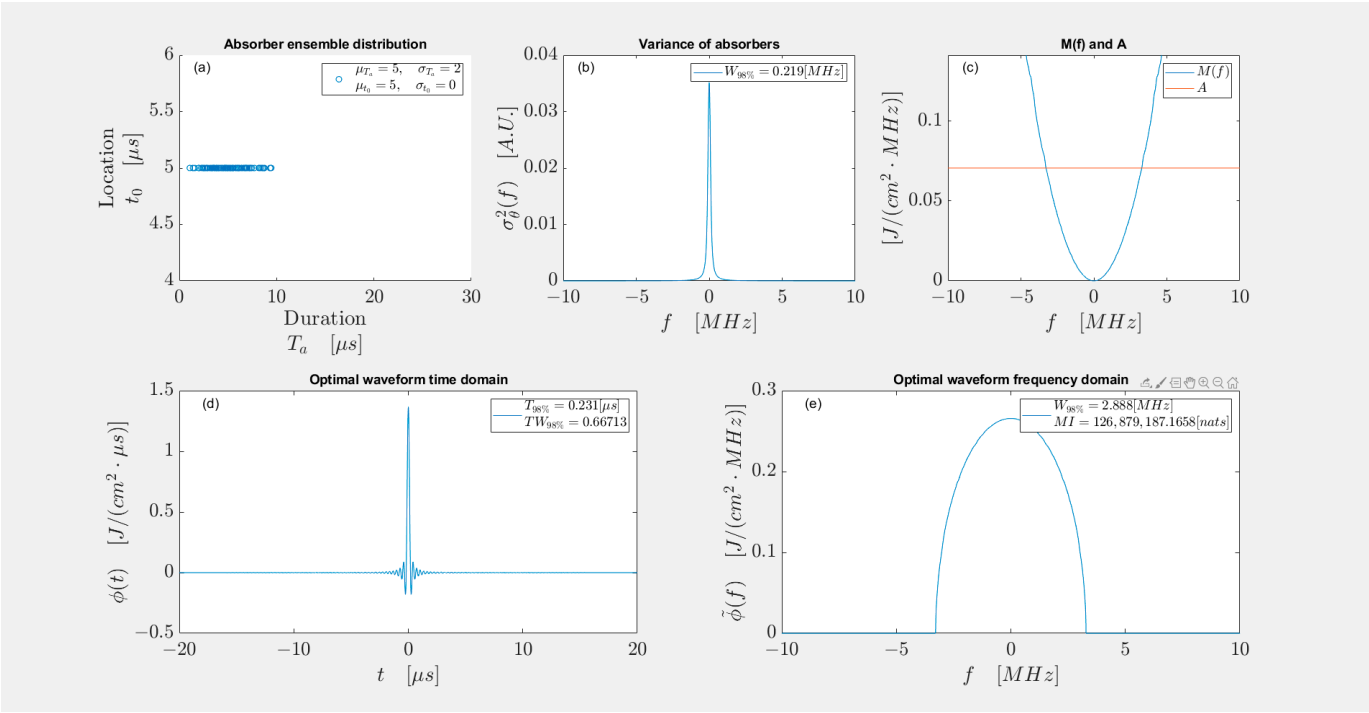

Figure 2. (**a**) Distribution of 100 absorber parameters; (**b**) Variance of absorber ensemble; (**c**) M(f) and A used in optimization problem; (**d**) Optimal waveform in time domain; (**e**) Optimal waveform in frequency domain.

Figure 2b shows the variance of the absorber ensemble $\sigma_\theta^2(f)$, which provides an intrinsic view of the frequency range where there is the most uncertainty (higher amplitude means higher uncertainty in that frequency). The spectral variance $\sigma_\theta^2(f)$ is the variance of all the absorbers' transfer functions $\widetilde{\theta}(f)$ at each frequency, calculated via Equation (27). Figure 2c shows $M(f) = \frac{P_{nn}(f)T_O}{2\sigma_\theta^2(f)}$ and the constant A used in the optimization algorithm. Figure 2c illustrates the terminology of the "water-filling" method. The idea is to 'waterfill'—that is for the optimal signal to put its energy where there is room in the allowable space between $M(f)$ and A. The input duration is a constraint of the problem, here this constraint is set to be smaller than the observation time $T_O = 20[\mu s]$ and the energy limit is calculated from Equation (37). We suppose that the energy limit is given by E (total amount of "water"), and that the $M(f)$ (the "bottle" to be filled) is fixed with a given noise level, input duration and absorber ensemble profile. The constant A ("water" level) is found when all the E amount of "water" (energy) is poured into the $M(f)$ "bottle". Hence, the magnitude spectrum of the optimal waveform $\left|\widetilde{\phi}(f)\right|^2$ is found by keeping $M(f)$ under the constant A. That is, the algorithm specifies that the optimal waveform is found by 'waterfilling' the allowable energy between $M(f)$ and A by putting the allowable energy in the frequencies that give the greatest increase in mutual information.

Figure 2e is one possible optimal waveform $\widetilde{\phi}(f)$ obtained by taking the square root of $\left|\widetilde{\phi}(f)\right|^2$. Note here that the optimal waveform is not unique, i.e., all waveforms that have a magnitude spectrum of $\left|\widetilde{\phi}(f)\right|^2$ are optimal. Figure 2d is the optimal waveform $\phi(t)$ in the time domain obtained by directly taking the inverse Fourier transform of the waveform $\widetilde{\phi}(f)$ in (e). The legends in Figure 2b,d,e show the corresponding energy concentration region. For example, in Figure 2d, 98% energy of the waveform $\phi(t)$ is concentrated in the time range $[-0.23\mu s, 0.23\mu s]$ which meets the duration constraint that the observation time $T_O = 20[\mu s]$ must be greater than $2T + T_a$. The absorber ensemble in this example ensemble has a mean duration of $T_a = 5[\mu s]$, so with this mean duration $2T + T_a = 5.46[\mu s]$. The absorber that has the longest duration in the ensemble has the duration $T_a = 11.33[\mu s]$, so in that case, $2T + T_a = 11.56[\mu s]$.

3.2. Trends in Uncertainty in Absorber Duration/Thickness

Consider an absorber ensemble with a small uncertainty in both duration and location, as shown in Figure 3a. All other parameters for absorber, input and noise are kept the same as the previous example in Section 3.1. However, the duration uncertainty is reduced in order to study the effect of uncertainty in duration. As can be seen in Figure 3b, compared with the previous example the variance of the absorber ensemble expands into a wider frequency range and the smaller uncertainty results in a smaller amplitude of $\sigma_\theta^2(f)$. Hence, the optimal waveform in Figure 3e tends to be more spread out in frequency compared to Figure 2e.

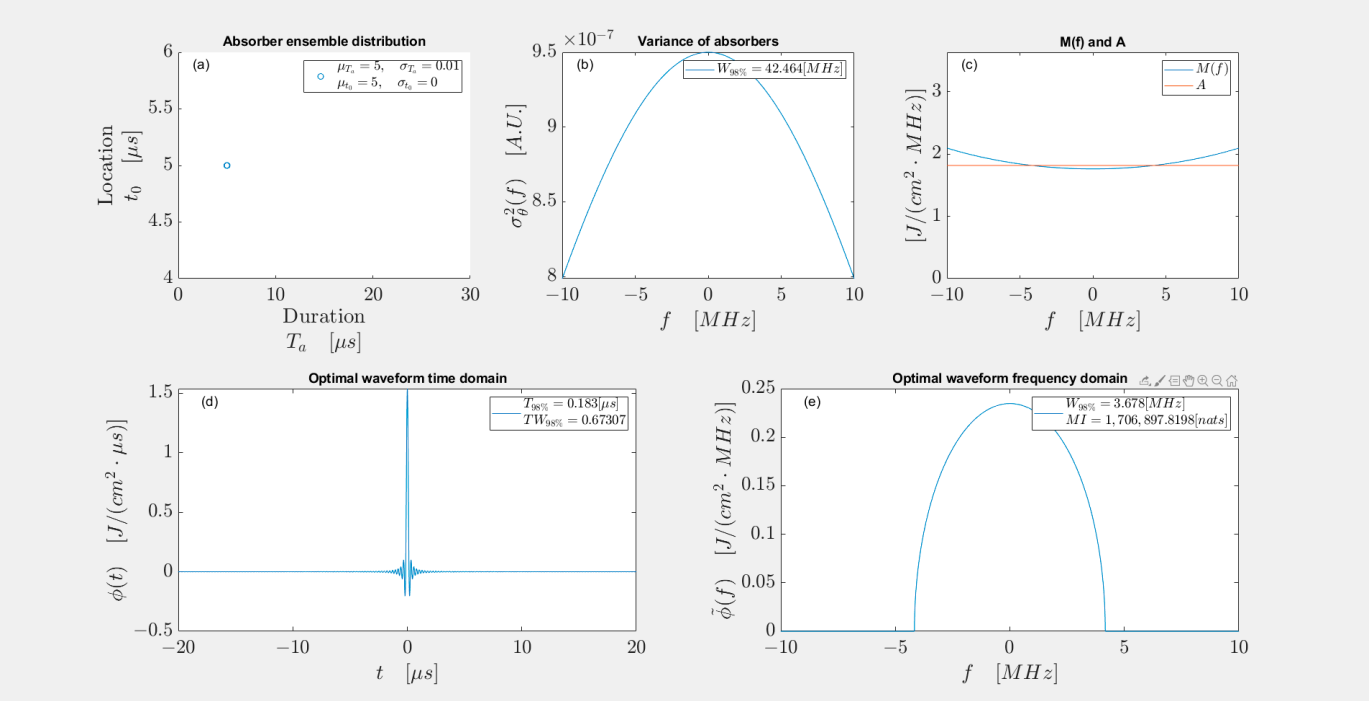

Figure 3. (**a**) Distribution of 100 absorber parameters; (**b**) Variance of absorber ensemble; (**c**) M(f) and A used in optimization problem; (**d**) Optimal waveform in time domain; (**e**) Optimal waveform in frequency domain.

To better illustrate this trend, Figure 4b plots the optimal waveform bandwidth change for various absorber duration standard deviations σ_{T_a}. In the small standard deviation for duration (σ_{T_a}) range, the optimal waveform narrows in frequency with higher uncertainty (amplitude) in absorber duration. This follows because the absorber ensemble variance $\sigma_\theta^2(f)$ narrows in frequency (but increases in amplitude) when the uncertainty on duration increases which can be seen from Figure 4a.

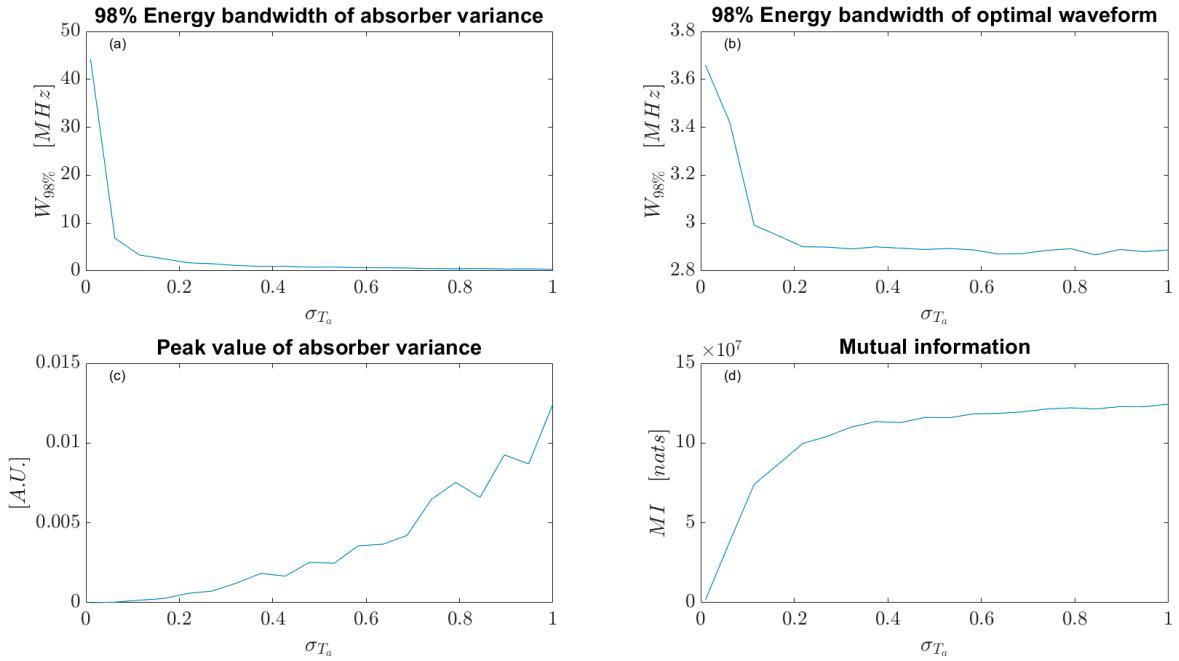

Figure 4. (**a**) 98% energy bandwidth of absorber variance; (**b**) 98% energy bandwidth of optimal waveform; (**c**) Peak value of absorber variance; (**d**) Mutual information obtained by optimal waveform.

The energy concentration of the variance of the absorber ensemble approaches zero (that is, very narrowly concentrated in frequency, although high in amplitude) when σ_{T_a} is large enough and hence the optimal waveform concentration reaches a near constant value. This can be explained clearly by looking at the plots in Figures 5 and 6, which show frequency domain plots of two ensembles' variances and real/imaginary parts of the absorbers in those ensembles. The ensemble in Figure 5 has less uncertainty in absorber duration (smaller σ_{T_a} which results in a lower (but wider range) amplitude of $\sigma_\theta^2(f)$ in Figure 5a compared with the ensemble in Figure 6 which has higher amplitude of $\sigma_\theta^2(f)$. Other parameters are the same (certain location $t_0 = 5[\mu s]$, mean duration $\mu_{T_a} = 5[\mu s]$).

The square absorbers are sinc functions in frequency, with amplitudes and zero crossings specified by their duration T_a in time, and oscillations in frequency related with their shift in time (location t_0). As can be seen in Figure 5b–d the absorbers with less duration uncertainty almost have almost the same frequency spectrum, because t_0 are the same and have small uncertainty in T_a—that is, there is very little variation between absorbers, they are all mostly the same and in the same location. Hence, the overall magnitude of the variance between the absorbers is small (the variance plot in Figure 5a is in 10^{-5} order of magnitude). However, a small difference between absorbers in the high frequency region has higher significance compared to the small overall variance magnitude and hence results in a wider variance $\sigma_\theta^2(f)$—that is, a wider variance in frequency with a lower peak value. Now consider the ensemble in Figure 6 which has higher uncertainty in absorber duration. The higher uncertainty manifests itself as different peak amplitude of the absorbers in plots (b), (c) and (d), giving a higher maximum amplitude of variance $\sigma_\theta^2(f)$, now on the order of 10^{-2}. The variance order of magnitude trend can also be seen from Figure 4c. The differences in the high frequencies of the absorber plots becomes comparatively insignificant and thus results in a concentrated variance $\sigma_\theta^2(f)$ (high max amplitude, narrower spread) in frequency. However, when the uncertainty on duration is big enough, the concentration of variance $\sigma_\theta^2(f)$ approaches zero and cannot be concentrated (narrowed) any further, even though the magnitude of $\sigma_\theta^2(f)$ can still increase with increasing uncertainty on absorber duration as shown in Figure 4c. That is, the behavior of $\sigma_\theta^2(f)$ approaches that of a delta

function and leads to an optimal waveform that must be concentrated in frequency as much as possible.

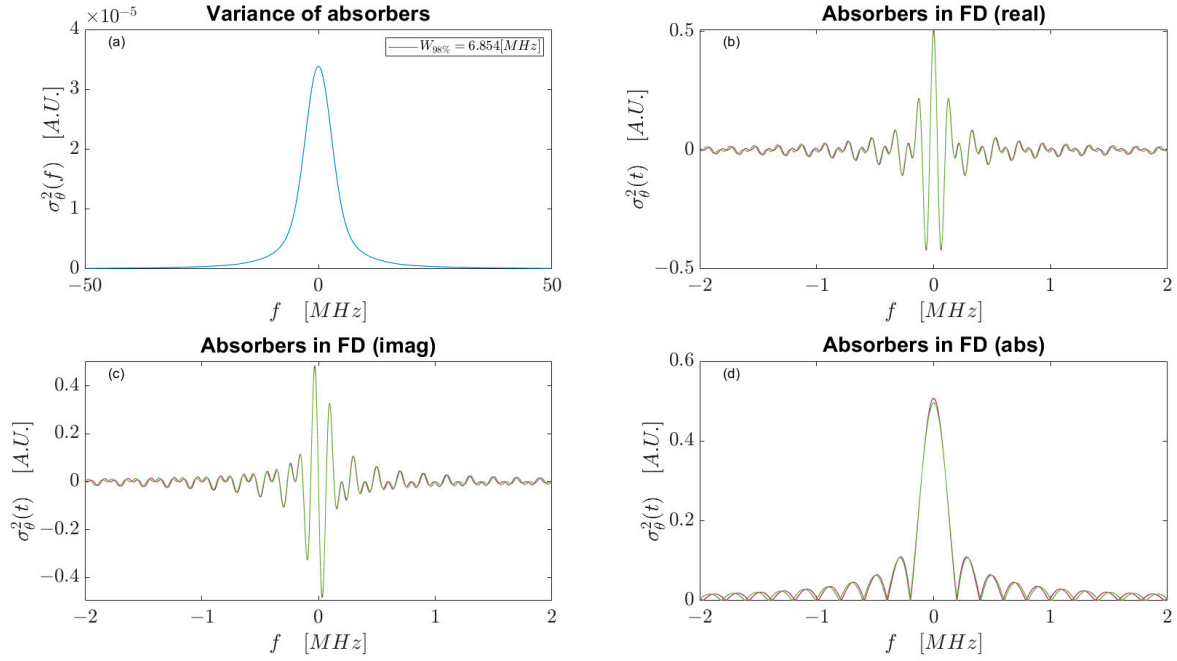

Figure 5. (**a**) Ensemble variance $\sigma_\theta^2(f)$ of 100 absorbers with same location $t_0 = 5[\mu s]$ and uncertain duration with mean $\mu_{T_a} = 5[\mu s]$ and standard deviation $\sigma_{T_a} = 0.0621[\mu s]$; (**b**) Real part of 5 absorbers in the ensemble; (**c**) Imaginary part of 5 absorbers in the ensemble; (**d**) Absolute value of 5 absorbers in the ensemble. Different colors in (**b**,**c**,**d**) represent different absorbers in the ensemble.

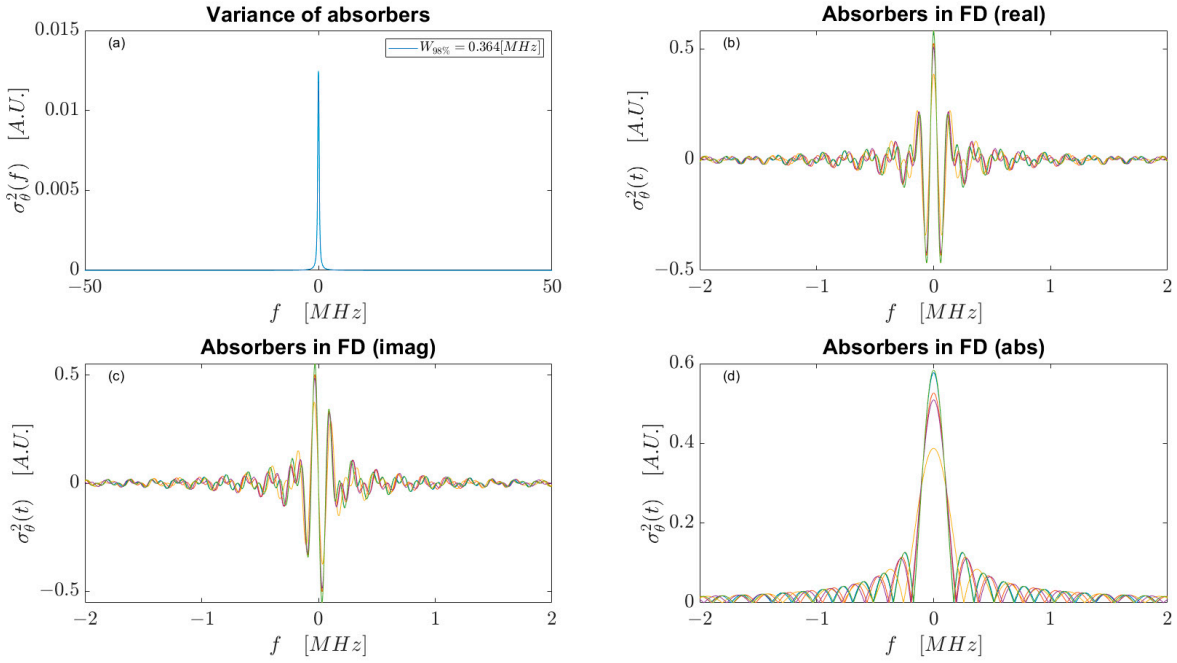

Figure 6. (**a**) Ensemble variance $\sigma_\theta^2(f)$ of 100 absorbers with same location $t_0 = 5[\mu s]$ and uncertain duration with mean $\mu_{T_a} = 5[\mu s]$ and standard deviation $\sigma_{T_a} = 1[\mu s]$; (**b**) Real part of 5 absorbers in the ensemble; (**c**) Imaginary part of 5 absorbers in the ensemble; (**d**) Absolute value of 5 absorbers in the ensemble. Different colors in (**b**–**d**) represent different absorbers in the ensemble.

It needs to be noted that the optimal waveform energy concentration frequency range is not the same as the ensemble variance energy concentration frequency range. The concentration of the optimal waveform energy is related to the ensemble variance $\sigma_\theta^2(f)$, the noise level $P_{nn}(f)$, available bandwidth W, observation time T_O, and the energy limit E, since the optimal waveform is obtained through

$$|\phi(f)|^2 = \max\left[0, A - \frac{P_{nn}(f)T_O}{2\sigma_\theta^2(f)}\right] \tag{42}$$

Figure 7 demonstrates the effect of the noise floor. Figure 7a–d plot the same ensemble variance with different noise floor $P_{nn}(f)$. The noise floor in Figure 7a is the same as the values used in previous simulations shown in this section. Figure 7b–d increase the noise floor $P_{nn}(f)$ by 100, 1000, and 10,000 times. The extreme values of $P_{nn}(f)$ are not realistic for photoacoustic imaging but are simulated to understand the effect of the noise floor. Figure 7e–h show the optimal waveform corresponding to the $P_{nn}(f)$ in (a) to (d). In Figure 7a–d, the bound where variance $\sigma_\theta^2(f)$ is greater than $P_{nn}(f)$ is shown by red circles, and the corresponding frequency range is printed on the legend. The bounds are shown for illustration only, since the units of $P_{nn}(f)$ and $\sigma_\theta^2(f)$ are not the same, hence comparing the actual values between them is meaningless. In Equation (42), the $\frac{P_{nn}(f)}{\sigma_\theta^2(f)}$ in the optimization algorithm acts like a (negative) weighting function in frequency, which implies that the optimal waveform allocates its energy where $\sigma_\theta^2(f)$ dominates (i.e., is large). At some frequencies, noise dominates or "buries" the variance (as shown in Figure 7 where the noise floor is high comparing to the variance of absorbers). In such cases, allocating energy to frequencies where noise dominates will only result in a small gain in information. As shown in Figure 7, as the noise floor increases, the frequency range where variance $\sigma_\theta^2(f)$ is above the noise floor becomes narrower, hence, the optimal waveform tends to be narrower. Furthermore, when the energy of the waveform is limited, the optimal waveform fills its energy in the frequency region near the peak of $\sigma_\theta^2(f)$ even if the noise floor is low, as shown in Figure 7a,e. The mutual information MI for all cases are calculated and shown in the legend in Figure 7 e–h. The value of the mutual information decreases with increasing noise level since the mutual information is proportional to $\frac{\sigma_\theta^2(f)}{P_{nn}(f)}$ as shown in Equation (29).

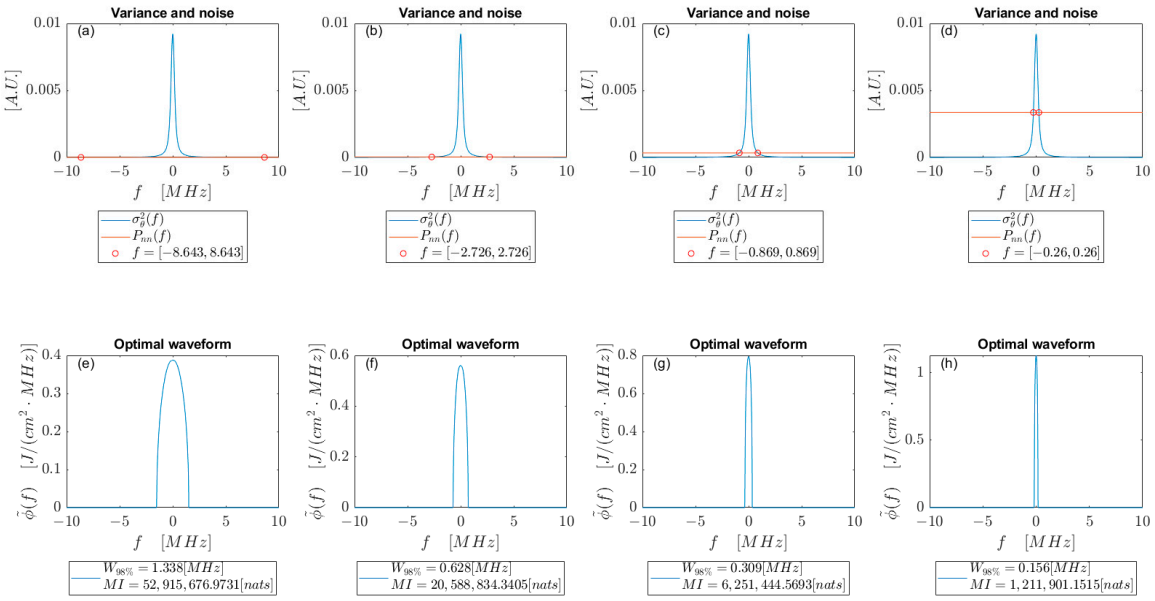

Figure 7. (**a**–**d**) Absorber ensemble variance and noise power spectrum; (**e**–**h**) Optimal waveform with corresponding noise floor.

Another way of looking at the problem of how noise and energy constraint affect the shape of the optimal waveform is to keep the noise constant and increase the energy constraint of the input waveform. To simulate this, twenty optimal waveforms corresponding to different energy constraints are found for an absorber ensemble with the same noise floor. The ensemble distribution and variance are shown in Figure 8a,b to provide a view of how the absorbers are distributed. The absorber ensemble shown in Figure 8a has known location $t_0 = 5[\mu s]$ and unknown durations/thicknesses with the distribution $\mu_{T_a} = 5[\mu s]$ and $\sigma_{T_a} = 1[\mu s]$. Noise spectrum is $P_{nn}(f) = 3.35 \times 10^{-4}\left[\mathrm{J/(cm^2 \cdot MHz)}\right]$.

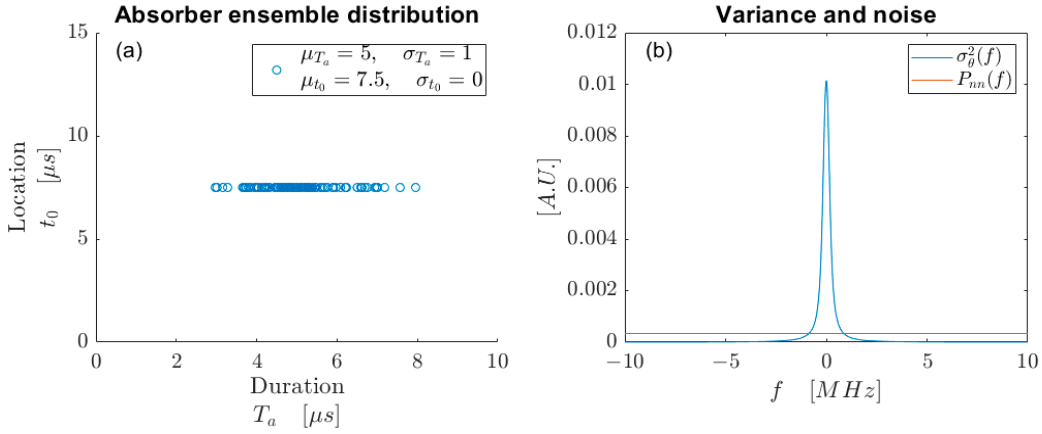

Figure 8. (**a**) Absorber ensemble parameter distribution; (**b**) Variance of absorber ensemble and illustrative noise floor.

Figure 9 shows nine of those optimal waveforms and the corresponding bandwidth and mutual information are shown in the legend. The optimal waveforms durations (constraint) are $T = 10[\mu s]$. Energy limit on the input waveform varies from $0.0309\left[\mathrm{J/cm^2}\right]$ (0.1 of the energy limit given by the safety standard) to $3.0929 \times 10^3\left[\mathrm{J/cm^2}\right]$ (10,000 times of the energy limit given by the safety standard).

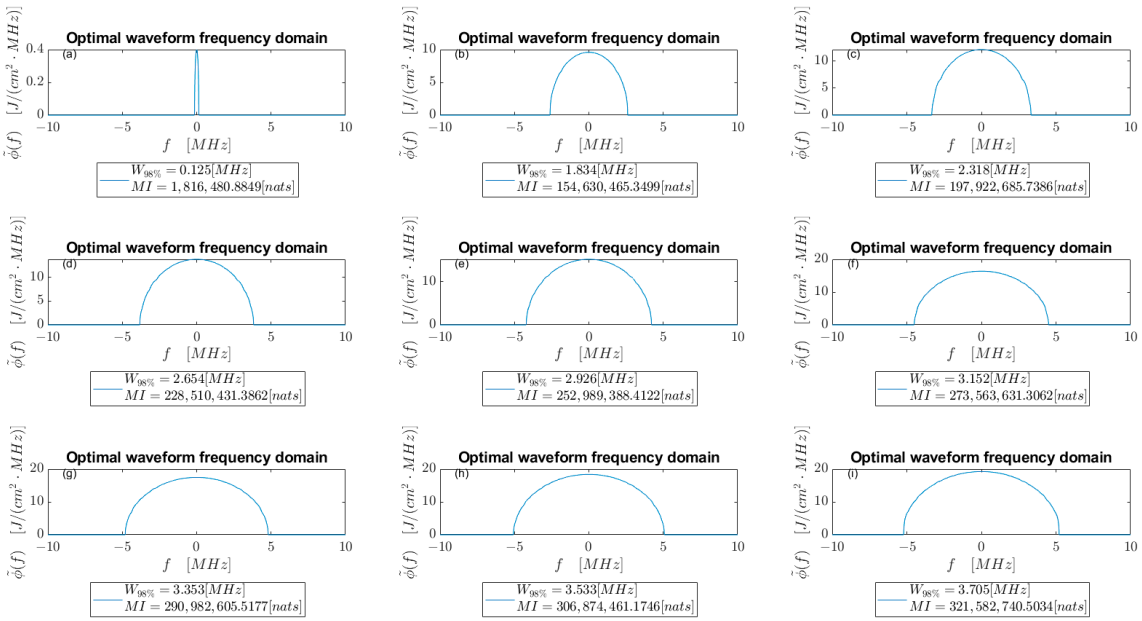

Figure 9. Optimal waveforms with different energy limitations. (**a**–**i**) Energy limitations from $0.0309\left[\mathrm{J/cm^2}\right]$ to $3.0929 \times 10^3\left[\mathrm{J/cm^2}\right]$.

From Figure 9, the optimal waveform tends to spread in frequency when the energy limit increases, i.e., more energy is devoted to the frequencies where $\frac{\sigma_\theta^2(f)}{P_{nn}(f)}$ is relatively small compared to the frequencies where ensemble variance $\sigma_\theta^2(f)$ peaks. To better illustrate this result, Figure 10a shows the relationship of the twenty optimal waveforms' bandwidth and the energy constraint. Figure 10b shows the relationship between the mutual information obtained by the twenty optimal waveforms and their energy limit.

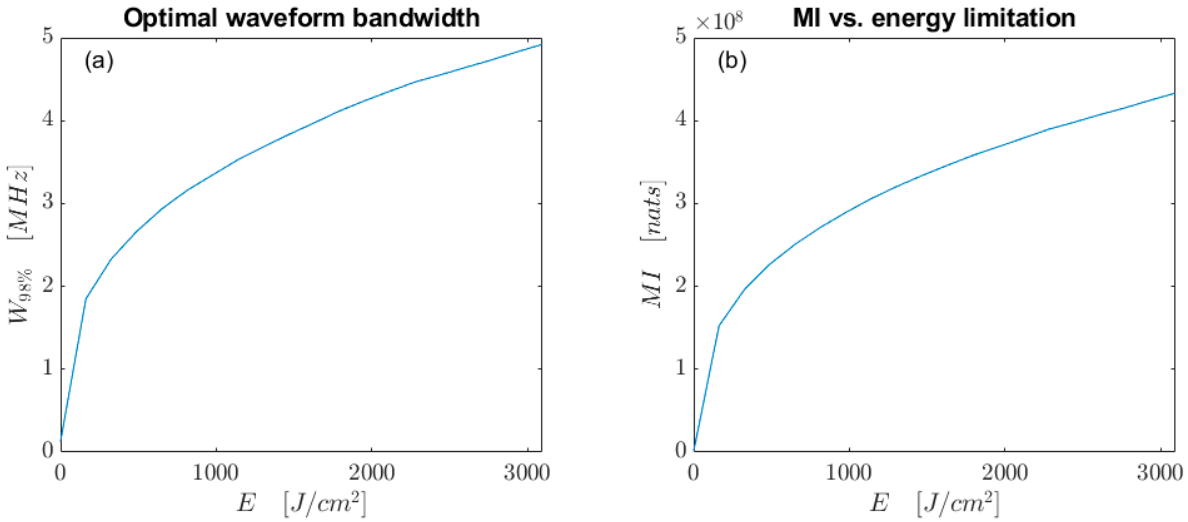

Figure 10. (**a**) Bandwidth of optimal waveforms change with energy limitation; (**b**) Mutual information obtained by optimal waveforms change with energy limitation.

From Figure 10a, the bandwidth of the optimal waveforms increases with increasing energy limit. The resultant mutual information, shown in Figure 10b, shows almost the same pattern. Moreover, even when the energy constraint changes drastically in Figure 10a, the optimal waveform concentrates in a relatively small bandwidth (several MHz). This implies that devoting energy to the frequencies where noise outweighs the variance of absorbers can only give minor mutual information; a better strategy to increase mutual information is to devote energy to the frequencies where variance is not outweighed by the noise.

3.3. Trends in Absorber Mean Duration (Size)

This section explores how the mean duration of the absorber ensemble affects the variance of the absorber ensemble and in turn affects the optimal waveform. Figure 11 shows the result of an ensemble of 100 absorbers. The distribution parameters of the ensemble are shown in Figure 11a which indicates a mild uncertainty in absorber duration and a large mean duration ($\mu_{T_a} = 10[\mu s]$). Another ensemble of 100 absorbers with the same uncertainty in duration but a small mean duration ($\mu_{T_a} = 0.1[\mu s]$) is analyzed in Figure 12. Other parameters used for Figures 11 and 12 are the same and listed here: observation duration is $T_O = 10[\mu s]$ and energy limit is calculated from the safety limit in Equation (37); noise level is low comparing to the variance but realistic for photoacoustic imaging applications $P_{nn}(f) = 3.35 \times 10^{-7}\left[\mathrm{J}/\left(\mathrm{cm}^2 \cdot \mathrm{MHz}\right)\right]$.

As shown in Figures 11 and 12, the peak value of variance $\sigma_\theta^2(f)$ increases with increasing mean duration, however, the variance concentration in frequency does not change significantly. To better see the trend, Figure 13 plots the absorber variance energy concentration, optimal waveform energy concentration, absorber variance peak value and mutual information against different absorber ensemble mean durations. Twenty ensembles are used in each subplot.

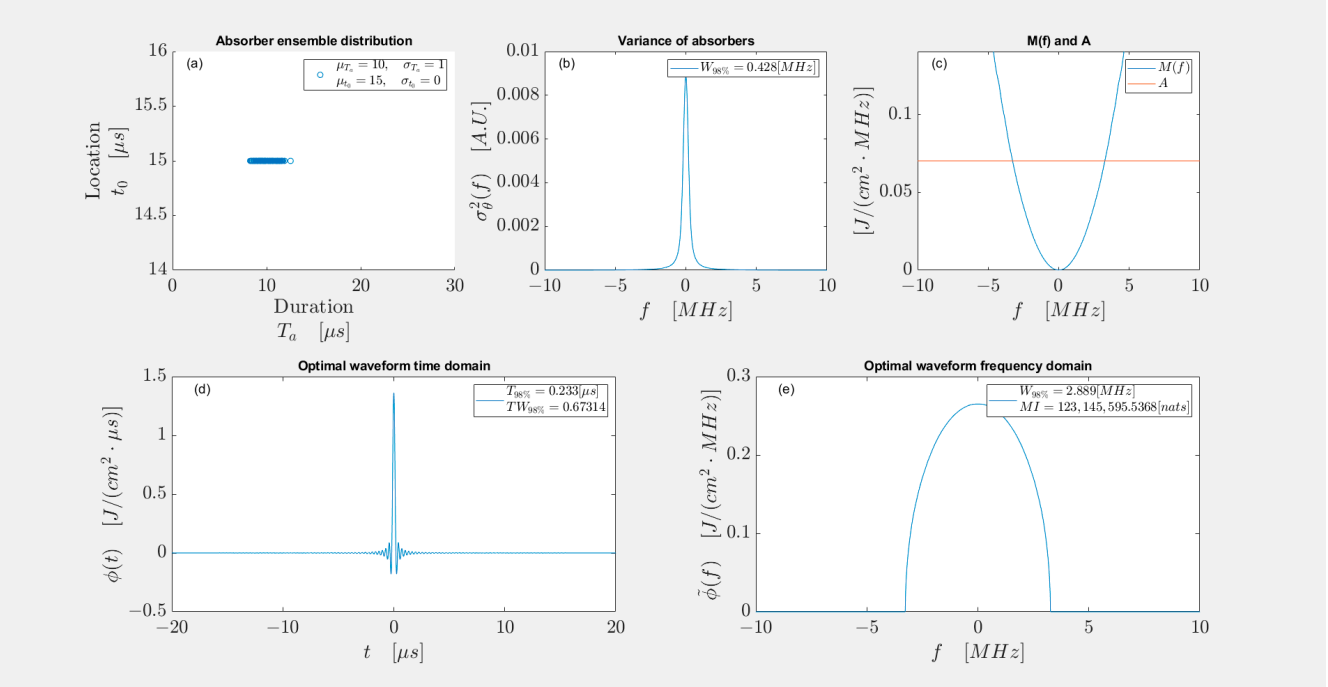

Figure 11. (**a**) Distribution of 100 absorber parameters; (**b**) Variance of absorber ensemble; (**c**) M(f) and A used in optimization problem; (**d**) Optimal waveform in time domain; (**e**) Optimal waveform in frequency domain.

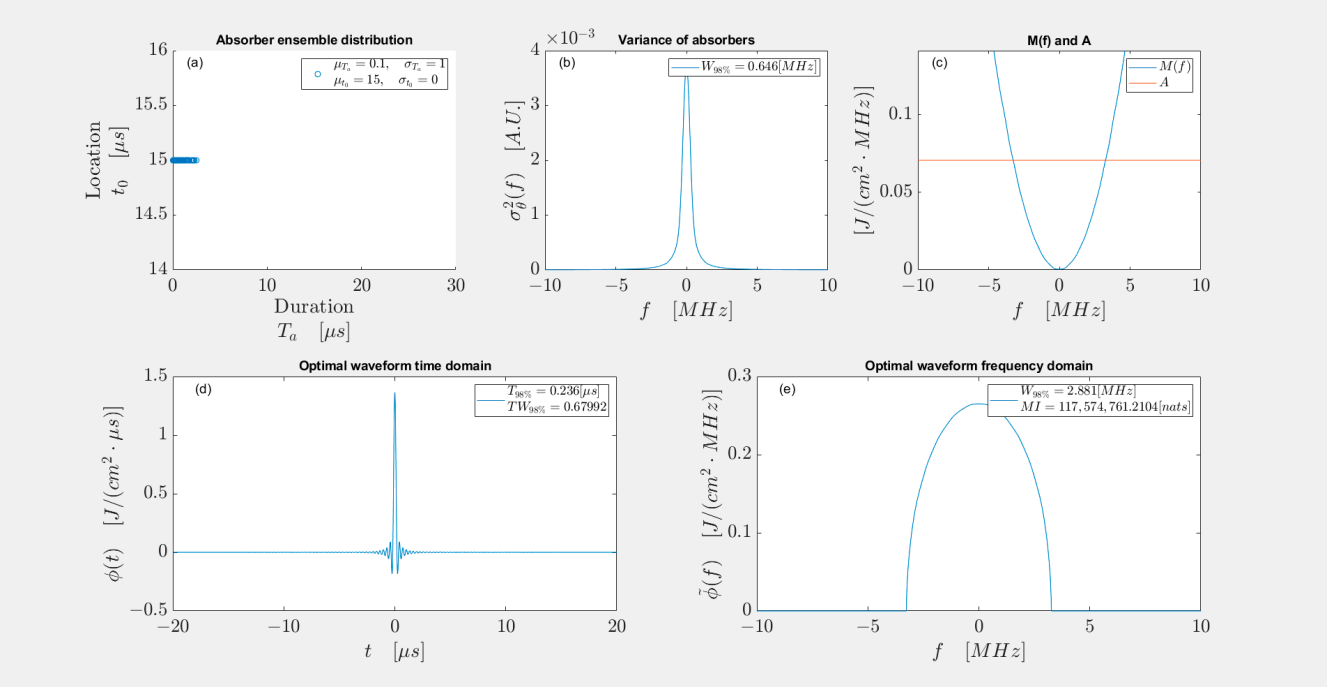

Figure 12. (**a**) Distribution of 100 absorber parameters; (**b**) Variance of absorber ensemble; (**c**) M(f) and A used in optimization problem; (**d**) Optimal waveform in time domain; (**e**) Optimal waveform in frequency domain.

As shown in Figure 13a, the absorber variance bandwidth does not change significantly with increasing absorber mean duration. From Figure 13c, the increase in variance peak value occurs at the small mean duration range and then remains almost constant with increasing mean duration. Compared with Figure 4c, which plots the peak values of

variance for a different ensemble with different uncertainties in duration, the change in Figure 13c is small. This is because the variance $\sigma_\theta^2(f)$ reveals the uncertainty in the absorbers. Furthermore Figure 13 demonstrates that the change in absorber variance is insignificant with increasing mean duration. Hence, the optimal waveform and the resulting mutual information do not have any significant change as shown by the almost flat lines in subplots (b) and (d).

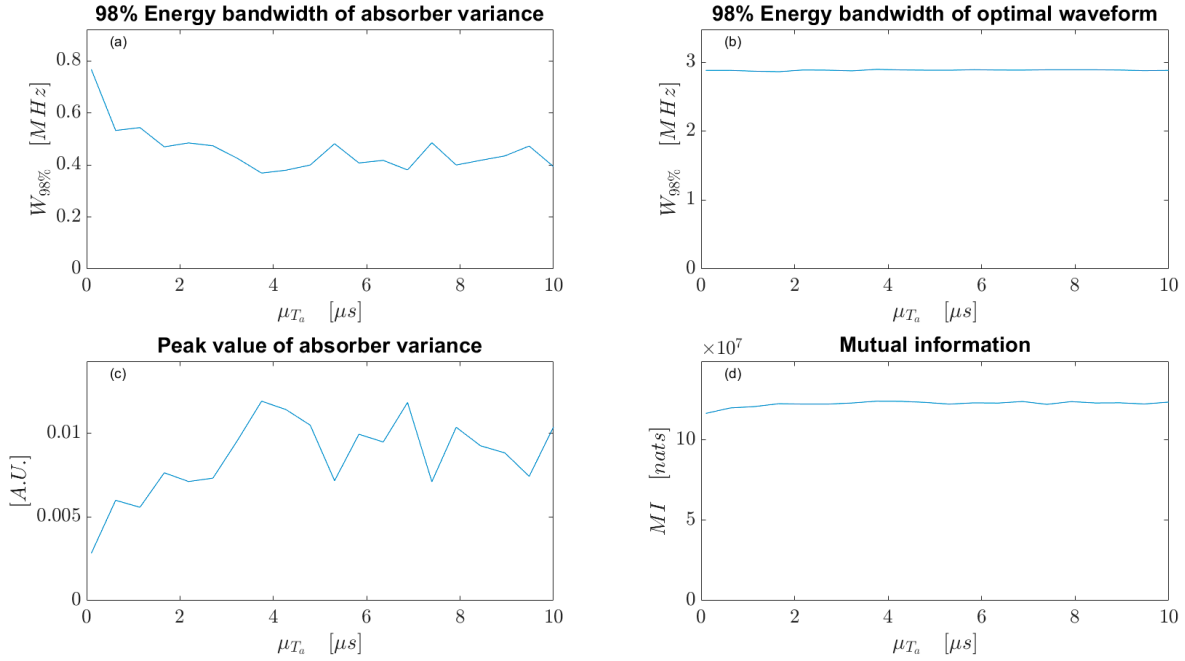

Figure 13. (**a**) 98% energy bandwidth of absorber variance; (**b**) 98% energy bandwidth of optimal waveform; (**c**) Peak value of absorber variance; (**d**) Mutual information obtained by optimal waveform.

To better illustrate the trend shown in Figures 13c, 14a and 15a show two absorber ensembles' variances $\sigma_\theta^2(f)$ with different mean durations but the same uncertainty. Subplots (b), (c) and (d) in Figures 14 and 15 show real, imaginary, and absolute values of five absorber transfer functions in the ensembles. Although the absorber transfer functions could change significantly with changes in mean duration (as shown in the absorber plots (b), (c) and (d) in Figure 14 for small mean duration and (b), (c) and (d) in Figure 15 for large mean duration), the uncertainty can still be similar (peak values from Figures 14a and 15a are similar).

3.4. Trends in Uncertainty in Absorber Location

This section considers different absorber ensembles consisting of 100 square absorbers with the same known duration $T_a = 5$ [µs] (absorber thickness is 7.5 [mm]). The locations of absorbers, expressed via t_0, are unknown and follow a Gaussian distribution with mean location $\mu_{t_0} = 7.5$ [µs] (mean distance to receiver is 11.2 [mm]), with different standard deviations for different ensembles. Figure 16a shows the absorber ensemble distribution with location standard deviation $\sigma_{t_0} = 0.06$ which is considered a small uncertainty.

Figure 16b shows the absorber ensemble variance in the frequency domain. Figure 16c shows the $M(f)$ and constant A found from the "water-filling" approach. Figure 16e is the corresponding optimal waveform in the frequency domain and Figure 16d is the optimal waveform in the time domain obtained through direct inverse Fourier transform of (e). As shown in Figure 16d,e, the optimal waveform can be viewed as a series of pulses in time, with spacing equal to the absorber duration T_a. Note here that the observation time T_O must capture all but negligible energy of the optimal waveform and additionally the absorber characteristic duration, i.e., $2T + T_a \leq T_O$. The observation time used in Figure 16

is $T_O = 30[\mu s]$, which is greater than the effective duration of the input waveform. The effective duration is calculated as the duration that contains 98% of the input energy. This 'effective duration' is adopted to account for waveforms that are theoretically never zero (for example, a sinc or a Gaussian never reach zero) but effectively have a finite duration. As shown in the legend in Figure 16d, the effective duration of the entire pulse train is approximately 15 micro seconds and 7 pulses are inside this effective duration. Figure 17 plots 4 of the pulses of separately (the pulse at the origin and 3 smaller pulses at the positive time axis because the entire pulse train is even). The effective duration ($T_{98\%}$) of each individual pulses and their amplitude (Amp) at their own center are shown in the legends. As shown in the detailed plots, it is obvious that the pulses are spaced by the $T_a = 5[\mu s]$. The effective duration of each pulse $T < 1[\mu s]$ is much less than the input duration constraint of $10[\mu s]$ and obeys $2T + T_a \leq T_O$. Figure 17 also shows the trend that the peaks become wider (larger effective duration) and smaller (absolute amplitude) as they get away from the origin.

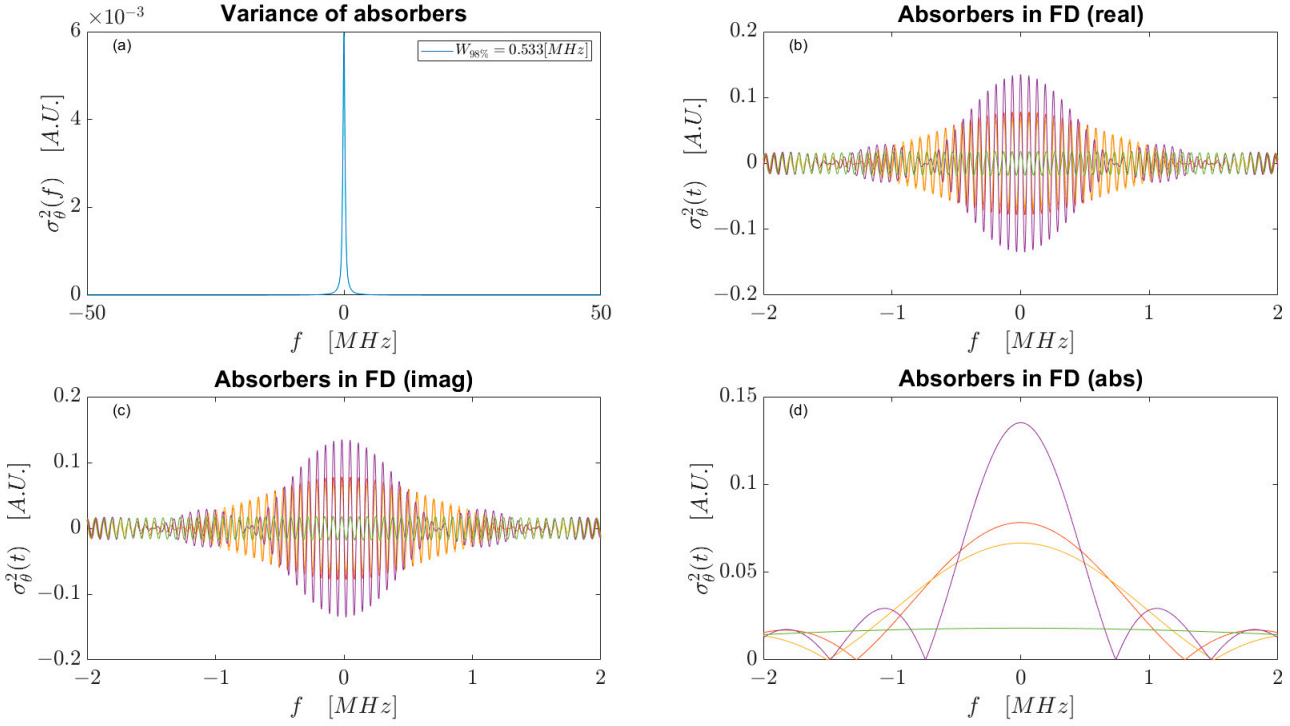

Figure 14. (**a**) Ensemble variance of 100 absorbers with same location $t_0 = 15[\mu s]$ and uncertain duration with mean $\mu_{T_a} = 0.1[\mu s]$ and standard deviation $\sigma_{T_a} = 1$; (**b**) Real part of 5 absorbers in the ensemble; (**c**) Imaginary part of 5 absorbers in the ensemble; (**d**) Absolute value of 5 absorbers in the ensemble. Different colors in (**b**,**c**,**d**) represent different absorbers in the ensemble.

We now consider a similar case where the uncertainty is absorber location is much larger. Figure 18 shows the simulation results of another absorber ensemble like the one shown in Figure 16. The difference is that now $\sigma_{t_0} = 1$, which indicates larger uncertainty in location compared to the case simulated in Figure 16. A similar trend is found in Figure 18. The optimal waveform is a series of pulses with the spacing equal to the absorber duration T_a and the detailed plots of individual pulses are shown in Figure 19. The effective durations of each pulses satisfy $2T + T_a \leq T_O = 30[\mu s]$. The trend of the pulses shows that the pulses become wider (larger effective duration) and smaller (absolute amplitude) as they get away from the origin.

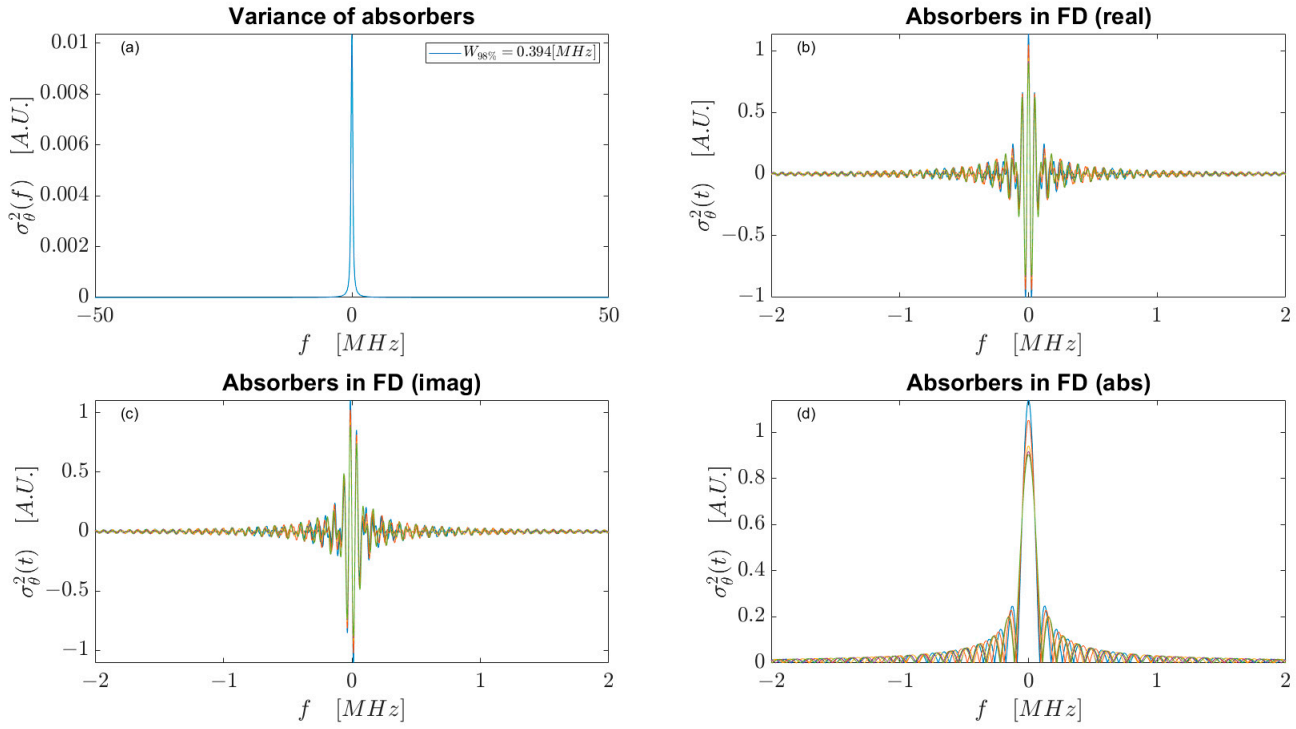

Figure 15. (**a**) Ensemble variance of 100 absorbers with same location $t_0 = 15[\mu s]$ and uncertain duration with mean $\mu_{T_a} = 10[\mu s]$ and standard deviation $\sigma_{T_a} = 1$; (**b**) Real part of 5 absorbers in the ensemble; (**c**) Imaginary part of 5 absorbers in the ensemble; (**d**) Absolute value of 5 absorbers in the ensemble. Different colors in (**b**,**c**,**d**) represent different absorbers in the ensemble.

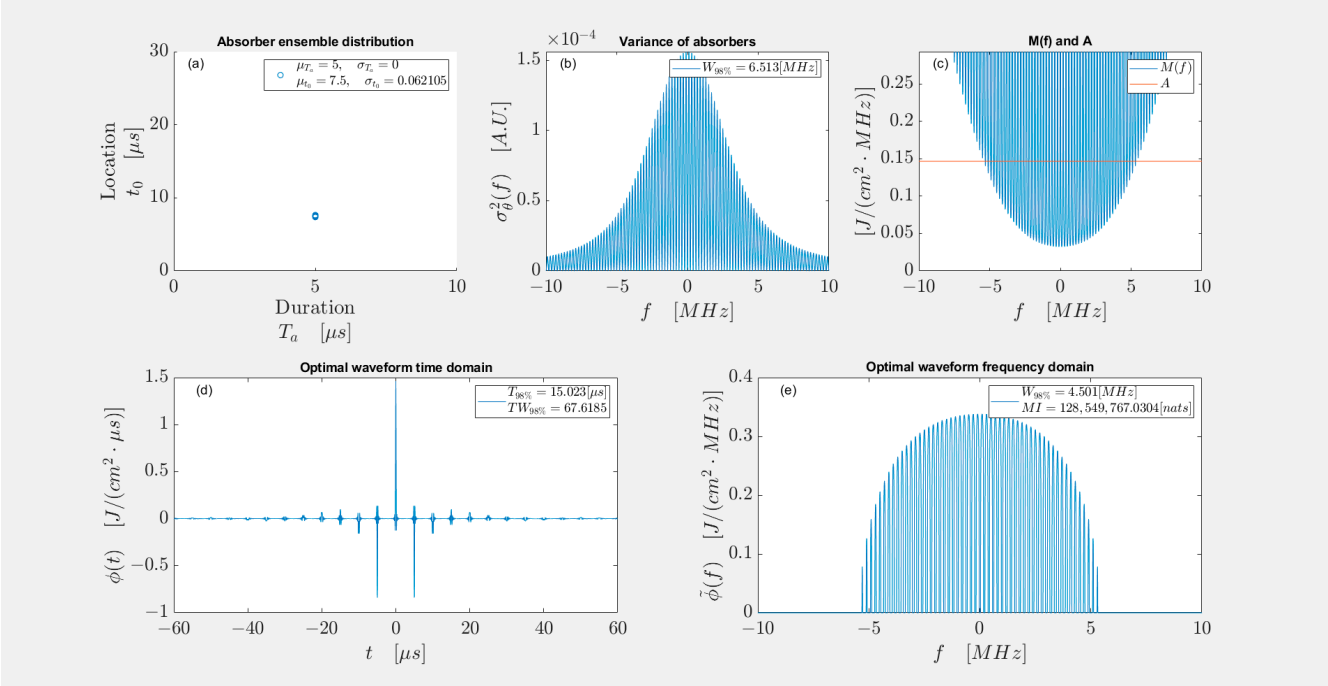

Figure 16. (**a**) Distribution of 100 absorber parameters; (**b**) Variance of absorber ensemble; (**c**) M(f) and A used in optimization problem; (**d**) Optimal waveform in time domain; (**e**) Optimal waveform in frequency domain.

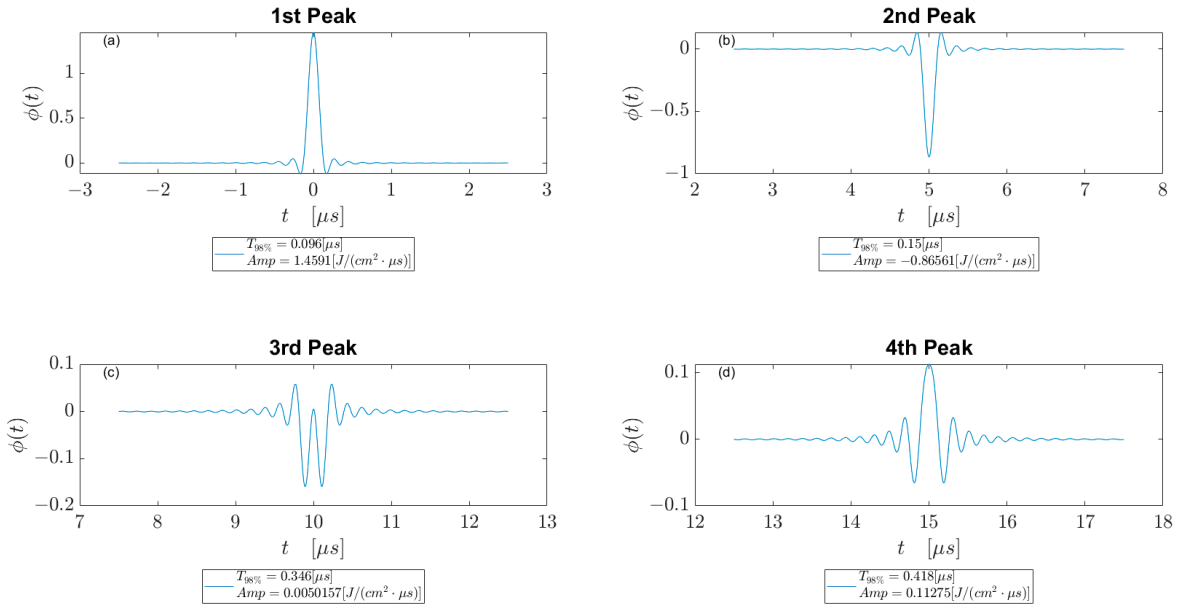

Figure 17. Separate plots of peaks of the time domain optimal waveform in Figure 16d. (**a**) Peak at origin; (**b**) Peak at 5 microsecond; (**c**) Peak at 10 micro second; (**d**) Peak at 15 micro second.

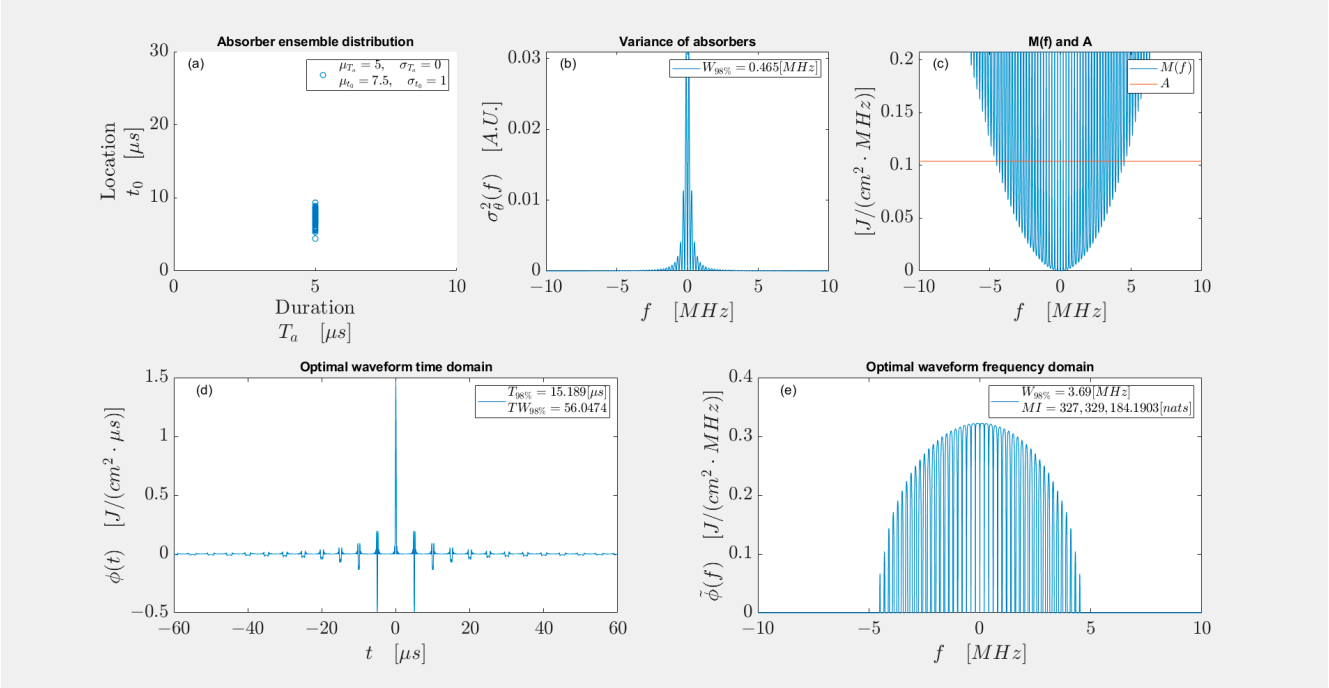

Figure 18. (**a**) Distribution of 100 absorber parameters; (**b**) Variance of absorber ensemble; (**c**) M(f) and A used in optimization problem; (**d**) Optimal waveform in time domain; (**e**) Optimal waveform in frequency domain.

From Figures 16–18, the absorber variance bandwidth decreases and amplitude increases with increasing uncertainty in location. Hence, the optimal waveform tends to be more compact in frequency (smaller range of frequencies).

The absorber variance is not the only component that affects the optimal waveform. These trends can be seen clearly in Figure 20 which calculates the characteristics of absorber variance and optimal waveform for twenty different ensembles with different uncertainties in location. The parameters used are the same as those used in Figure 16 except for the

location standard deviation σ_{t_0}, which indicates the uncertainty of location. As shown in Figure 20, in the small duration standard deviation σ_{T_a} range (small uncertainty on absorber duration), the optimal waveform narrows in frequency when there is higher uncertainty on absorber location. This follows because the absorber ensemble variance $\sigma_\theta^2(f)$ narrows in frequency when the uncertainty on location increases, Figure 20a. The (energy concentrated) bandwidth of the absorber ensemble variance $\sigma_\theta^2(f)$ tends to decrease/narrow to near zero when uncertainty in the absorber location is large enough, while the maximum amplitude increases. The reader is reminded that large uncertainty results in higher amplitude of ensemble variance $\sigma_\theta^2(f)$ as shown in Figure 20c. This result for uncertainty in location is the same as the result for uncertainty in duration. As a reminder from Figure 4a,c, when the uncertainty in absorber duration increases, the bandwidth of absorber ensemble variance $\sigma_\theta^2(f)$ tends to narrow to near zero and the amplitude increases. The observations in Figure 18 can be further explained by Figures 21 and 22.

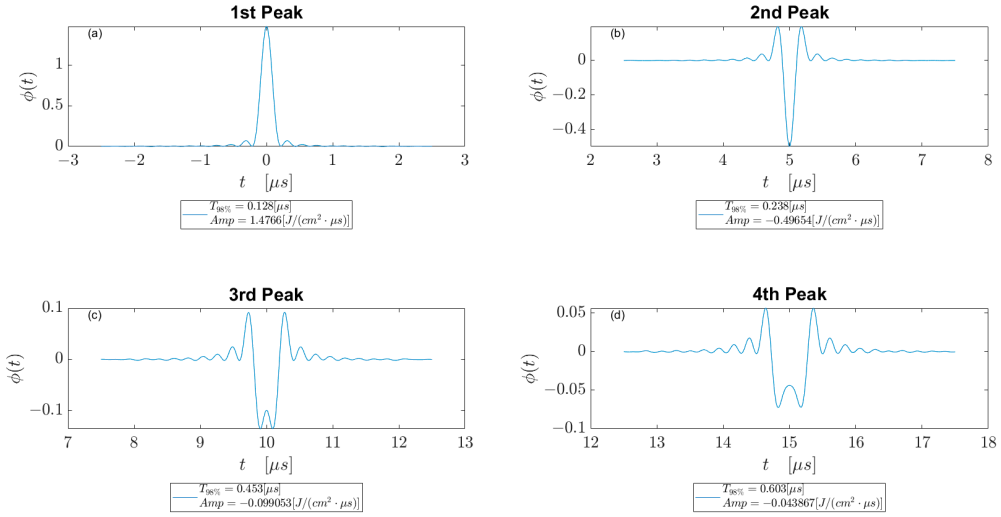

Figure 19. Separate plots of peaks of the time domain optimal waveform in Figure 18d. (**a**) Peak at origin; (**b**) Peak at 5 microsecond; (**c**) Peak at 10 micro second; (**d**) Peak at 15 micro second.

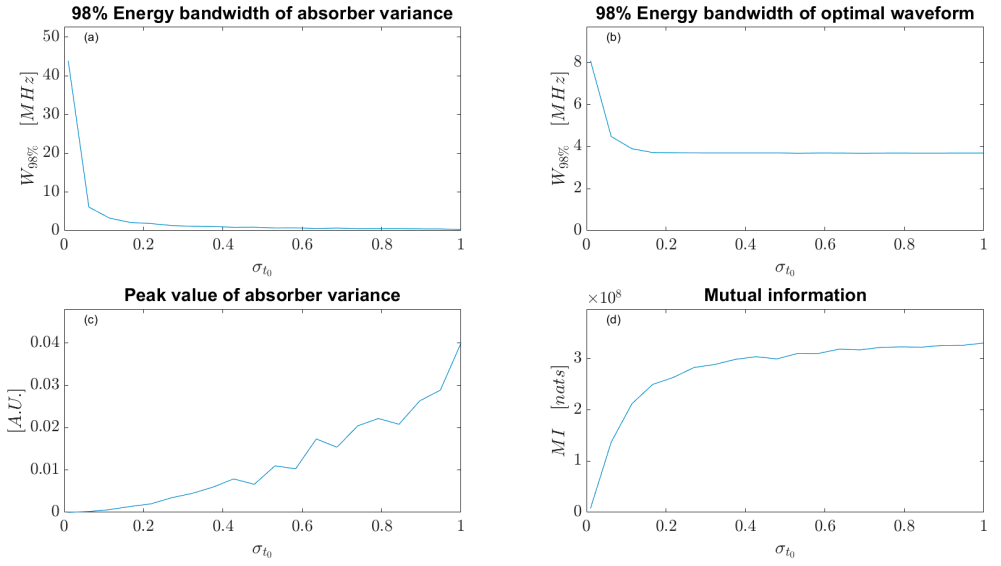

Figure 20. (**a**) 98% energy bandwidth of absorber variance; (**b**) 98% energy bandwidth of optimal waveform; (**c**) Peak value of absorber variance; (**d**) Mutual information obtained by optimal waveform.

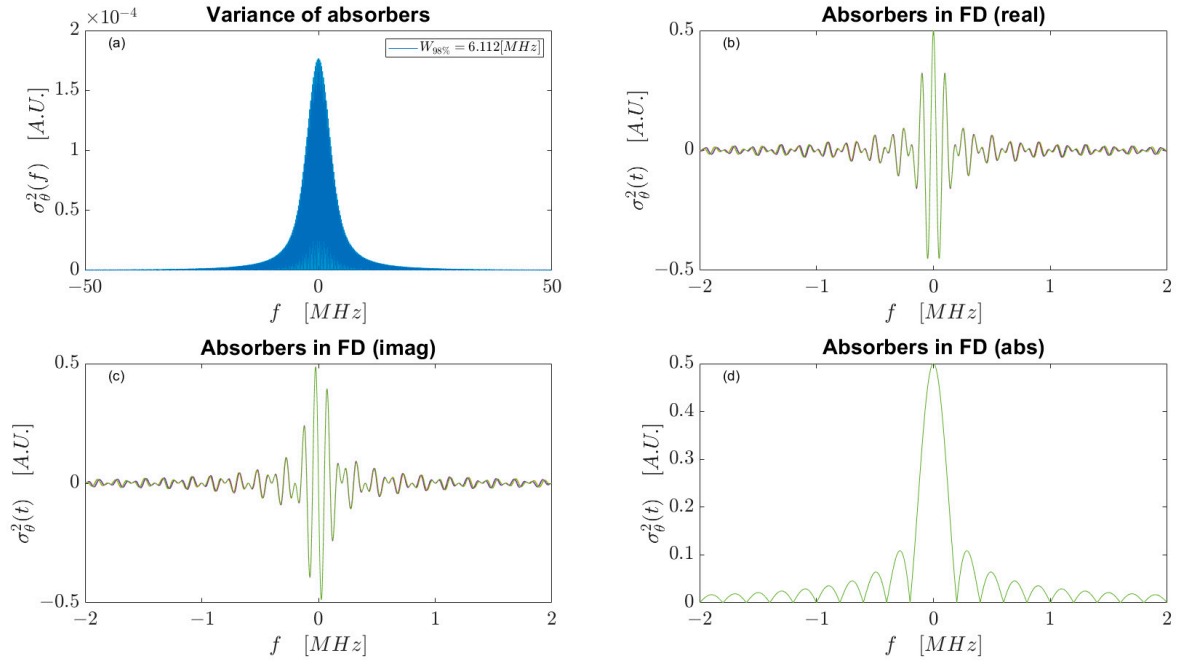

Figure 21. (**a**) Ensemble variance of 100 absorbers with same duration $T_a = 5[\mu s]$ and uncertain location with mean $\mu_{t_0} = 7.5[\mu s]$ and standard deviation $\sigma_{t_0} = 0.06$; (**b**) Real part of 5 absorbers in the ensemble; (**c**) Imaginary part of 5 absorbers in the ensemble; (**d**) Absolute value of 5 absorbers in the ensemble. Different colors in (**b**–**d**) represent different absorbers in the ensemble.

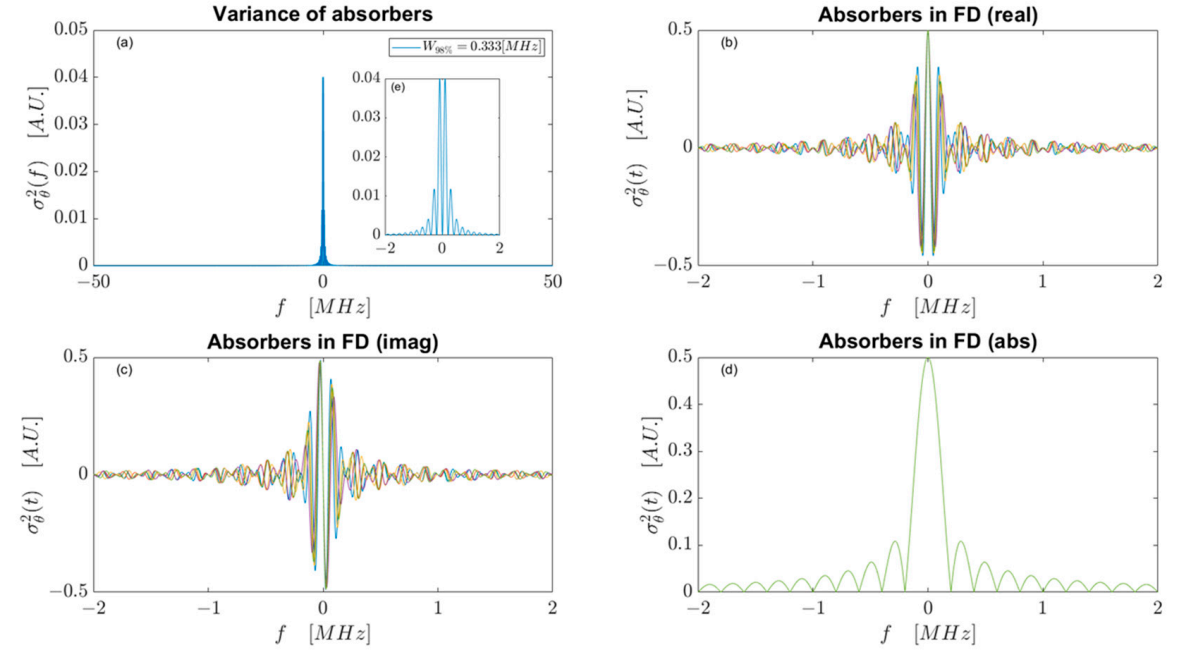

Figure 22. (**a**) Ensemble variance of 100 absorbers with same duration $T_a = 5[\mu s]$ and uncertain location with mean $\mu_{t_0} = 7.5[\mu s]$ and standard deviation $\sigma_{t_0} = 1$; (**b**) Real part of 5 absorbers in the ensemble; (**c**) Imaginary part of 5 absorbers in the ensemble; (**d**) Absolute value of 5 absorbers in the ensemble; (**e**) Zoomed plot of ensemble variance in (**a**). Different colors in (**b**–**d**) represent different absorbers in the ensemble.

Figures 21 and 22 show frequency domain plots of two ensembles' variances and real/imaginary parts of the absorbers in those ensembles. The ensemble in Figure 21 has less uncertainty in absorber location (smaller standard deviation σ_{t_0} of location which

results in a lower amplitude of ensemble variance $\sigma_\theta^2(f)$ in Figure 21a) than the ensemble in Figure 22 which has higher amplitude of $\sigma_\theta^2(f)$. Other parameters are the same (known duration $T_a = 5[\mu s]$, mean location $\mu_{t_0} = 7.5[\mu s]$) Note that square absorbers in time are sinc functions in frequency. The amplitudes and zero crossings of the sinc in frequency are specified by the duration of the absorbers T_a in time, whereas oscillations and phase in frequency are controlled by their shift in time (here, the shifts in time correspond to changes in location t_0). As can be seen in Figure 21b–d absorbers with less uncertainty have almost the same frequency spectrum, especially in the frequency range near the origin. Hence, the variance between the absorbers transfer functions is small (the variance plot in Figure 21a is in 10^{-4} order of magnitude). However, a small difference in the high frequency region (due to slight difference in location t_0 and the resulting difference in phase information shown by the real and imaginary plots) has high significance compared to the small overall variance and hence results in a wide spread of variance $\sigma_\theta^2(f)$. Consider the case in Figure 22, which has higher uncertainty in the absorber location than Figure 21. The higher uncertainty (different sidelobe amplitude of the absorbers in plot (b), (c)) gives variance $\sigma_\theta^2(f)$ with higher magnitude, on the order of 10^{-2}. The differences in the high frequencies of the absorber spectrum become insignificant, which lead to a concentrated variance $\sigma_\theta^2(f)$ in frequency. The results in Figures 21 and 22 explain the observations made from Figure 20, which indicated that higher uncertainty in location leads to concentrated (narrower) variance $\sigma_\theta^2(f)$ in frequency and hence a compact optimal waveform in frequency.

However, unlike the uncertainty in duration shown in Figure 4 and its explanation in Figures 5 and 6, in which we showed the ensemble variance $\sigma_\theta^2(f)$ comes from the difference in amplitude of absorber transfer functions, the uncertainty in location implies uncertainty in phase information of the absorber ensemble which manifests itself as oscillations in the sidelobes of the real and imaginary components of the absorber plots. These in turn contribute to the ensemble variance $\sigma_\theta^2(f)$. This can also be seen in Figure 22e which shows the ensemble variance zoomed in $[-2\text{MHz}, 2\text{MHz}]$. The variance peaks at the sidelobes of the absorbers. Hence, even though the magnitude plots of absorbers are the same for different absorbers in the ensemble (shown by Figure 22c), the variance of the absorbers can still be large, indicating large uncertainty. When the uncertainty on location is large enough, the concentration (frequency spread) of variance $\sigma_\theta^2(f)$ approaches zero and cannot be concentrated any further. However, the magnitude of $\sigma_\theta^2(f)$ can still increase with increasing uncertainty on absorber duration, as shown in Figure 20c.

3.5. Trends in Absorber Mean Location

This section demonstrates the effect of the mean location of absorbers μ_{t_0} on absorber variance and hence the effect on optimal waveform. Similar to the trend for absorber mean duration, the change in mean location plays a minor role in the absorber variance because it does not change the uncertainty about the absorbers.

Figures 23 and 24 show simulation results for absorber ensembles with the same known duration $T_a = 2[\mu s]$ and uncertain location, with different mean locations but the same uncertainty $\sigma_{t_0} = 1$. Other parameters (parameter for optimal waveform constraints and noise) are the same, and $T_O = 10[\mu s]$.

In Figures 23 and 24, the optimal waveforms are series of pulses with the spacing equal to the absorber duration T_a due to the uncertainty in location. From Figure 23 to Figure 24, the absorber variance shown in subplots (b) do not reveal visible changes compared to the significant change in mean location (from 3 to 15 microseconds). Hence, the optimal waveforms in Figures 23 and 24 are nearly the same. These trends can be seen clearly in Figure 25 which calculates the characteristics of absorber variance and optimal waveform for twenty different ensembles with same location uncertainties but different mean locations.

As can be seen from Figure 25, as the mean location of the absorber location increases, all metrics for absorber variance and optimal waveforms shown in subplots (a) to (d) are

almost a flat line. This leads to the conclusion that the change in mean location plays a minor role in the absorber variance because it does not change the uncertainty of absorbers.

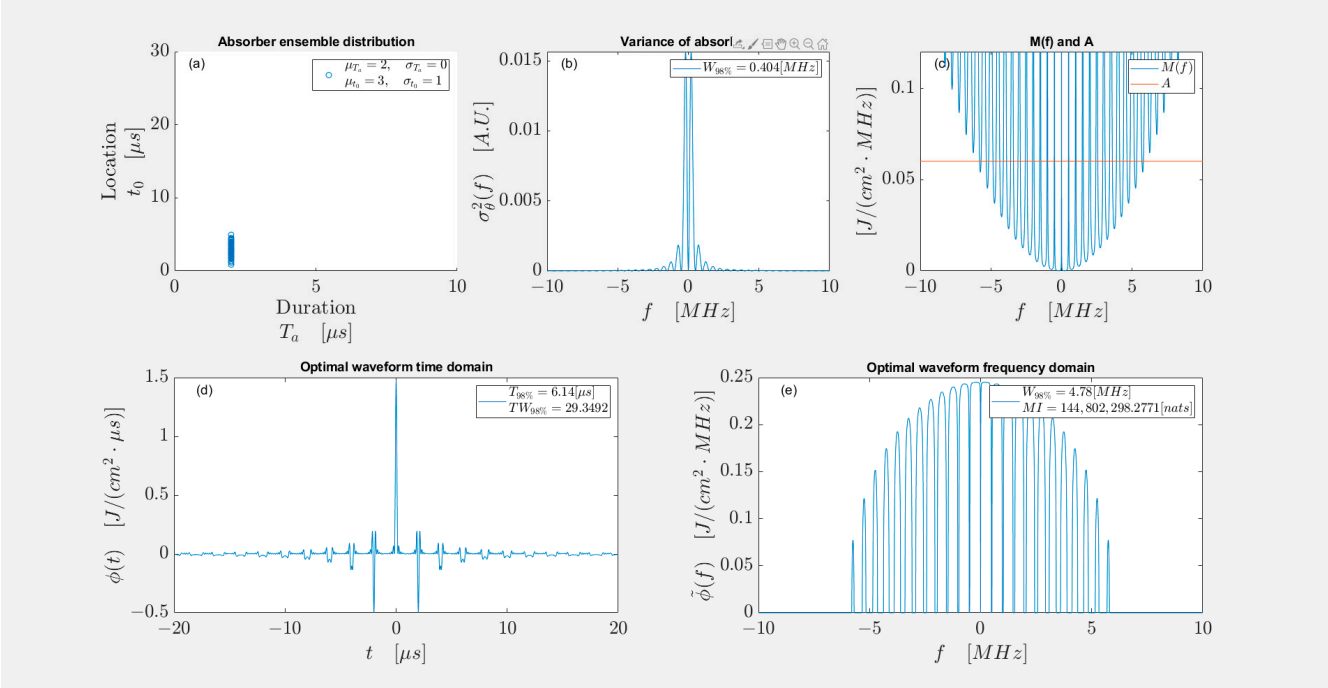

Figure 23. (**a**) Distribution of 100 absorber parameters; (**b**) Variance of absorber ensemble; (**c**) M(f) and A used in optimization problem; (**d**) Optimal waveform in time domain; (**e**) Optimal waveform in frequency domain.

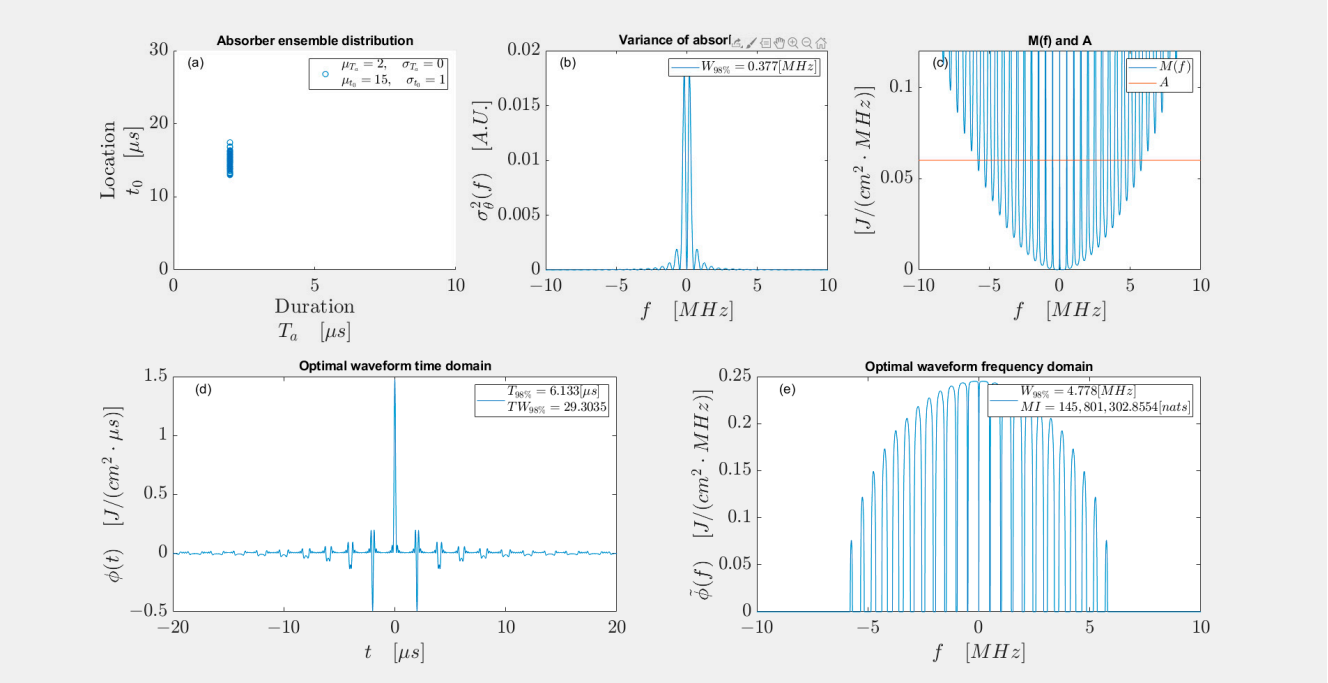

Figure 24. (**a**) Distribution of 100 absorber parameters; (**b**) Variance of absorber ensemble; (**c**) M(f) and A used in optimization problem; (**d**) Optimal waveform in time domain; (**e**) Optimal waveform in frequency domain.

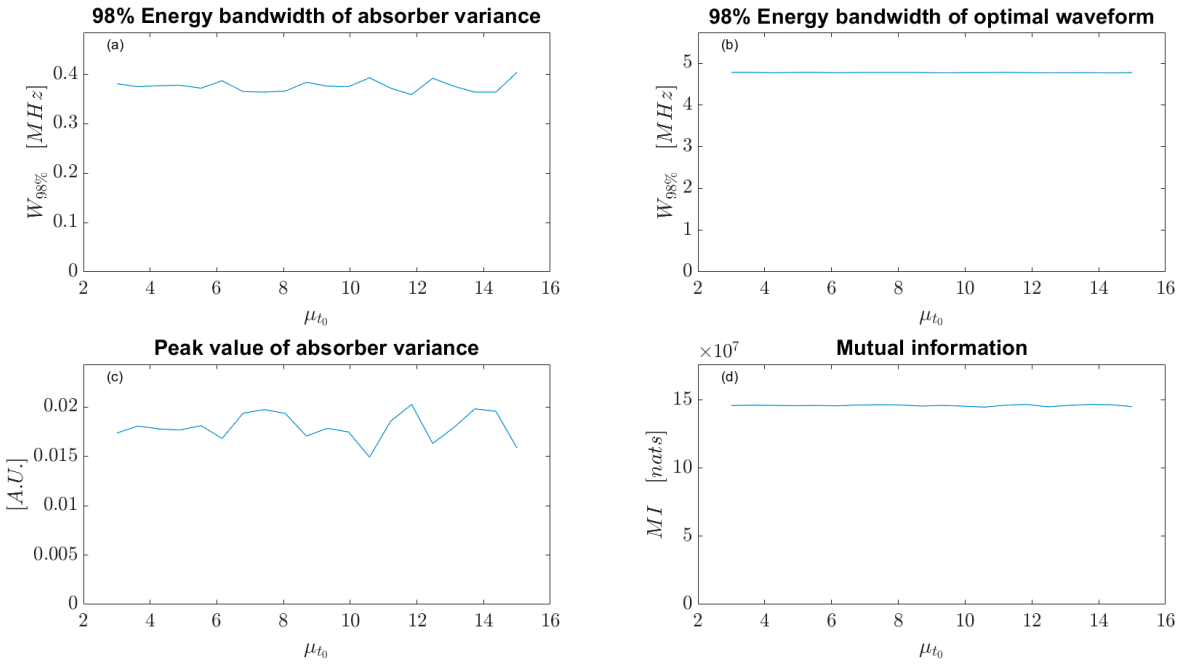

Figure 25. (**a**) 98% energy bandwidth of absorber variance; (**b**) 98% energy bandwidth of optimal waveform; (**c**) Peak value of absorber variance; (**d**) Mutual information obtained by optimal waveform.

3.6. Realistic Case When Duration and Location Are Both Uncertain

This section considers a realistic case when both duration and location of absorbers are uncertain. To gain insight, 400 absorber ensembles are generated. The absorber ensembles have the same mean duration $\mu_{T_a} = 5[\mu s]$ and mean location, $\mu_{t_0} = 7.5[\mu s]$. The input duration constraints are kept the same as previous simulations at $T = 10[\mu s]$. Observation durations also kept the same at $T_O = 20[\mu s]$. The energy limit is kept constant and calculated through Equation (37). Noise level is relatively low with the (realistic) value $P_{nn}(f) = 3.35 \times 10^{-7}\left[\mathrm{J}/\left(\mathrm{cm}^2 \cdot \mathrm{MHz}\right)\right]$. The absorber ensembles have different uncertainties; their parameters standard deviations are in the ranges $\sigma_{T_a} = 0.01..1$ and $\sigma_{t_0} = 0.01..1$.

Figure 26 shows the simulation results of the absorber ensemble with the largest uncertainty. As shown in Figure 26a, the absorber parameters are scattered in both location and duration dimensions. From Figure 26d,e, the corresponding optimal waveform combines the characteristics of the optimal waveforms for uncertain duration (Figure 2 which shows a single pulse shape in time and no oscillations in frequency) and uncertain location (Figure 18 which shows multiple pulses in time with spacing equal to the mean duration of absorbers, and oscillations in frequency).

Energy concentration trends of the absorber variance and optimal waveform and corresponding mutual information are shown in Figure 27.

As shown in Figure 27a, the bandwidth of absorber variance is large when uncertainty (no matter in duration or location) of the absorbers is small (σ_{T_a} and σ_{t_0} are close to zero). Hence, the resulting optimal waveform also spreads its energy in a larger bandwidth as shown in Figure 27b, where the (98% energy-concentrated) bandwidth $W_{98\%}$ peaks. In this small uncertainty region, the reason for the wide spread of the bandwidth of absorber variance and bandwidth of optimal waveform was explained via simulations of absorber transfer functions in previous sections. Simply put, when there is less uncertainty in the absorber (duration or location), a small difference in the amplitude of sidelobes of absorber transfer functions is significant compared to the amplitude difference in the main lobe (for duration uncertainty) or first sidelobe (for location uncertainty). Hence, the bandwidths of the absorber variance and corresponding optimal waveform spread in frequency. The bandwidth of the absorber variance drops quickly to near zero when uncertainties of

absorbers increase, which indicates the main difference between the absorbers in the ensemble is at zero frequency (peak of the absorber transfer function). The peak value of the variance of absorbers increases with increasing uncertainty (location or duration) of absorber, as shown in Figure 27c. However, with limited input energy, the mutual information also reaches a maximum value when uncertainty of absorber increases, as shown in Figure 27d.

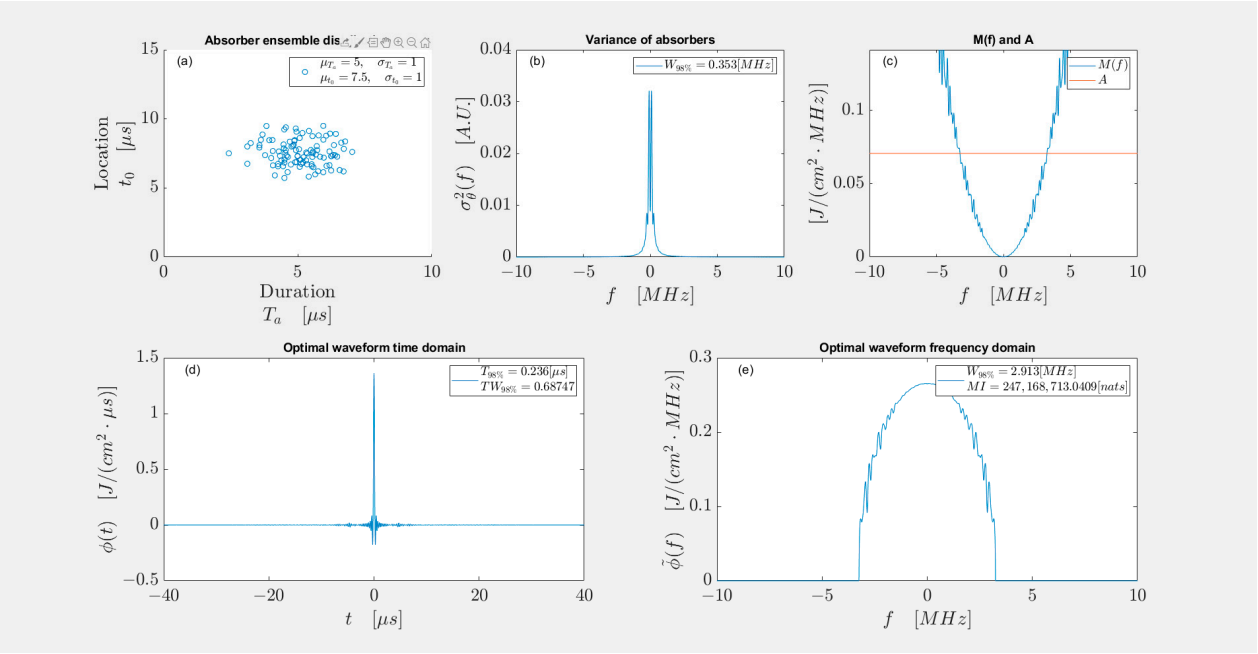

Figure 26. (**a**) Distribution of 100 absorber parameters; (**b**) Variance of absorber ensemble; (**c**) M(f) and A used in optimization problem; (**d**) Optimal waveform in time domain; (**e**) Optimal waveform in frequency domain.

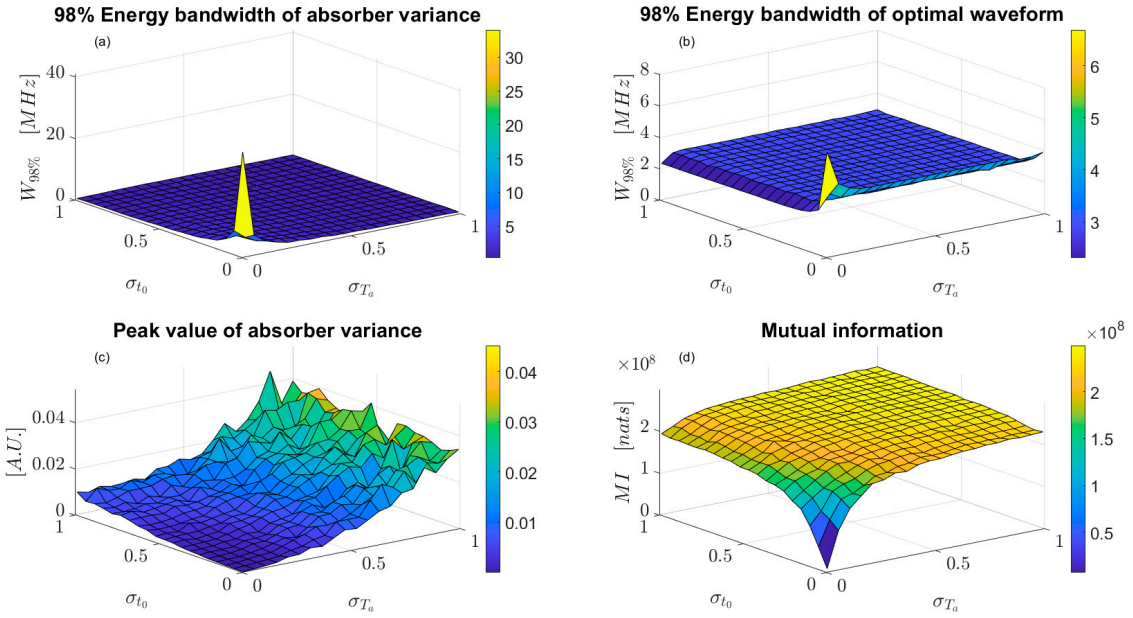

Figure 27. (**a**) 98% energy bandwidth of absorber variance; (**b**) 98% energy bandwidth of optimal waveform; (**c**) Peak value of absorber variance; (**d**) Mutual information obtained by optimal waveform.

3.7. Comparison with Optimal Waveforms for Detection and Other Commonly Used Waveforms

There are many different waveforms used in photoacoustics for different purposes, such as chirps for enhancing resolution [14], and specific optimal waveforms for SNR [9]. PSWFs and their discrete relative DPSS were found to be near optimal waveforms for SNR [10]. This section compares the optimal waveform for estimation obtained in this paper with other waveforms that are commonly used: the waveforms (PSWFs) obtained for near optimal detection (SNR) are chosen according to the process in [10]; the nanosecond pulse that is commonly used in photoacoustics [38]; and the chirp chosen according to the process in [14] to achieve high SNR and axial resolution for an absorber that has the duration of 5[μs] and at a location of 7.5[μs]. The goal of this section is to demonstrate how different goals affect the requirements for energy allocation on the input waveform. It is noted that the optimal waveform for SNR and the chirp require prior information of a deterministic absorber.

Figure 28 compares the optimal waveform for estimation with the other waveforms. Figure 28a shows the absorber ensemble with uncertain location and duration. The mean location is $\mu_{t_0} = 7.5[\mu s]$ and the mean duration is $\mu_{T_a} = 5[\mu s]$. The uncertainty of the absorber ensembles is described via the duration standard deviation $\sigma_{T_a} = 1$ and location standard deviation $\sigma_{t_0} = 1$. The constraints for input durations for the optimal waveform, the chirp, and PSWF are the same $T = 10[\mu s]$. Observation duration is $T_O = 20[\mu s]$. Energy limits for all waveforms are kept the same and calculated through Equation (37). Noise level is $P_{nn}(f) = 3.35 \times 10^{-7}\left[\mathrm{J}/\left(\mathrm{cm}^2 \cdot \mathrm{MHz}\right)\right]$. The PSWF shown in Figure 28 is obtained by the method in [10] to have near optimal SNR of a square absorber.

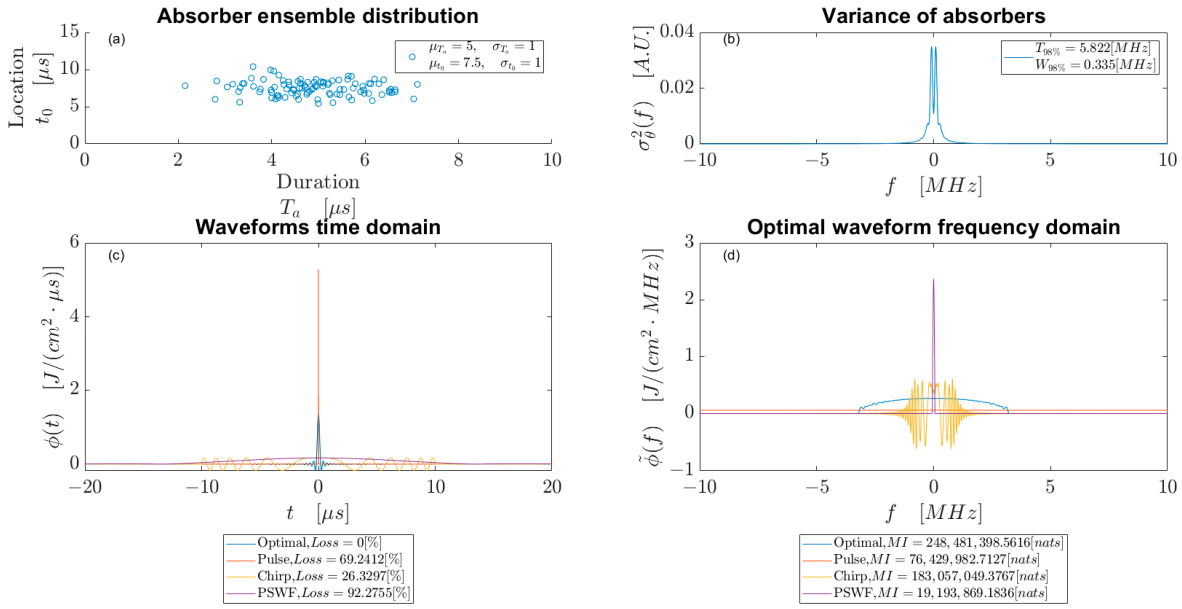

Figure 28. (**a**) Distribution of 100 absorber parameters; (**b**) Variance of absorber ensemble; (**c**) Optimal waveform for estimation and near optimal waveform for detection (PSWF) in time domain; (**d**) Optimal waveform for estimation and near optimal waveform for detection (PSWF) in frequency domain.

As shown in Figure 28, the near optimal waveform for detection (optimal SNR) tends to concentrate its energy as much as possible around the origin in the frequency domain to obtain the maximum response (SNR). On the other hand, the optimal waveform for estimation tends to spread its energy to a larger frequency range to obtain maximum information (parameter estimation). As shown in the legend of Figure 28c,d, the information loss of using a detection waveform is over 90%. The other two waveforms (short pulse and chirp) are neither optimal for detection nor optimal for estimation. The short pulse in time, due to the symmetry properties of the Fourier Transform between time and frequency

domains, spreads its energy in frequency too much to the frequencies where the information gain is small. The chirp, although concentrating its energy to the frequency range similar to the optimal waveform for estimation, does not allocate its energy in an optimal way. Hence, their information loss results are better than the PSWF but still not comparable with the optimal waveform for estimation. These simulations underscore the importance of articulating the waveform design goal (detection or estimation, or other purpose) and then designing the waveform accordingly. What is an optimal waveform for one objective is not optimal for another objective and, as the simulations show, may create a large performance loss for the other objective.

4. Conclusions

This paper uses information theory in photoacoustic imaging waveform design to obtain optimal waveforms for parameter estimation. From the simulation results, the conclusions are summarized below.

- The optimization algorithm allocates the input waveform energy to the frequencies where absorber ensemble variance $\sigma_\theta^2(f)$ dominates over the noise $P_{nn}(f)$ (water-filling). The ensemble variance $\sigma_\theta^2(f)$ essentially contains the information that is available. Increasing the input waveform energy limitation gives higher obtained mutual information. However, putting energy at frequencies where noise $P_{nn}(f)$ dominates only results in a small increase in obtained mutual information. Similarly, an increase of the noise floor will result in more information 'buried' by the noise. Hence, the obtained mutual information decreases.
- Uncertainty in absorber parameters plays an important role in the ensemble variance $\sigma_\theta^2(f)$. Higher uncertainty (no matter in duration or location) results in an absorber ensemble variance $\sigma_\theta^2(f)$ that has higher amplitude and is more concentrated in frequency. Uncertainty in duration (thickness) of absorbers typically results in a variance $\sigma_\theta^2(f)$ with a single peak centered at zero frequency. Uncertainty in absorber location (distance from receiver) typically results a variance $\sigma_\theta^2(f)$ with multiple peaks, with most of the energy concentrated near zero frequency. The characteristics of the absorber variance $\sigma_\theta^2(f)$ indicate where (in frequency) there is uncertainty about the absorber and hence where to allocate energy in the input waveform.
- The proposed algorithm returns the power spectrum of the optimal estimation waveform. The applicable time domain optimal waveform can be obtained through direct inverse Fourier transform of the square root of the obtained optimal power spectrum $|\phi(f)|^2$ given by the optimization algorithm. The optimal waveform is not unique, since the algorithm returns the power spectrum of the optimal waveform and not the optimal waveform itself. There are many possible waveforms that will correspond to the same power spectrum. It should also be noted that most of the energy of the resulting time domain waveform needs to be inside the observation duration.
- From the results for optimal waveforms, the shape of the optimal waveform depends on the uncertainty in different parameters. Uncertainty in duration requires the input waveform to be a single pulse in time, while uncertainty in location requires the input waveform in the time domain to be a pulse train with pulse spacings equal to the absorber durations. The shape of the optimal waveform for uncertainty in both duration and location requires the input waveform to be a combination of the two types of waveforms. In general, higher uncertainty (no matter in duration or location) needs the optimal waveform to be more concentrated in frequency to a certain minimum bandwidth, because the absorber variance generally always concentrates around zero frequency.
- From comparison with 'detection' waveforms and other waveforms, the estimation waveforms need to cover more frequencies where the information is contained. The proposed algorithm clearly demonstrates how different goals (detection or estimation) necessitate different input energy allocation methods, which in turn implies different types of waveforms.

Author Contributions: Conceptualization, N.B.; funding acquisition, N.B.; investigation, Z.S.; resources, N.B.; software, Z.S.; validation, Z.S.; writing—original draft, Z.S.; writing—review and editing, N.B. All authors have read and agreed to the published version of the manuscript.

Funding: This research was funded by Natural Sciences and Engineering Research Council of Canada (NSERC), grant number RGPIN-2023-03392.

Data Availability Statement: Data are contained within the article.

Conflicts of Interest: The authors declare no conflicts of interest. The funders had no role in the design of the study; in the collection, analyses, or interpretation of data; in the writing of the manuscript; or in the decision to publish the results.

References

1. Suzuki, K.; Yamashita, Y.; Ohta, K.; Kaneko, M.; Yoshida, M.; Chance, B. Quantitative Measurement of Optical Parameters in Normal Breasts Using Time-Resolved Spectroscopy: In Vivo Results of 30 Japanese Women. *J. Biomed. Opt.* **1996**, *1*, 330–334. [CrossRef] [PubMed]
2. Wells, P.N.T. Ultrasonic Imaging of the Human Body. *Rep. Prog. Phys.* **1999**, *62*, 671. [CrossRef]
3. Kruger, R.A.; Reinecke, D.R.; Kruger, G.A. Thermoacoustic Computed Tomography–Technical Considerations. *Med. Phys.* **1999**, *26*, 1832–1837. [CrossRef] [PubMed]
4. Kruger, R.A.; Kopecky, K.K.; Aisen, A.M.; Reinecke, D.R.; Kruger, G.A.; Kiser, W.L. Thermoacoustic CT with Radio Waves: A Medical Imaging Paradigm. *Radiology* **1999**, *211*, 275–278. [CrossRef] [PubMed]
5. Ku, G.; Wang, L.V. Scanning Thermoacoustic Tomography in Biological Tissue. *Med. Phys.* **2000**, *27*, 1195–1202. [CrossRef] [PubMed]
6. Xu, M.; Wang, L.V. Time-Domain Reconstruction for Thermoacoustic Tomography in a Spherical Geometry. *IEEE Trans. Med. Imaging* **2002**, *21*, 814–822. [CrossRef] [PubMed]
7. Xu, M.; Xu, Y.; Wang, L.V. Time-Domain Reconstruction Algorithms and Numerical Simulations for Thermoacoustic Tomography in Various Geometries. *IEEE Trans. Biomed. Eng.* **2003**, *50*, 1086–1099. [CrossRef] [PubMed]
8. Telenkov, S.A.; Alwi, R.; Mandelis, A. Photoacoustic Correlation Signal-to-Noise Ratio Enhancement by Coherent Averaging and Optical Waveform Optimization. *Rev. Sci. Instrum.* **2013**, *84*, 104907. [CrossRef]
9. Baddour, N.; Sun, Z. Photoacoustics Waveform Design for Optimal Signal to Noise Ratio. *Symmetry* **2022**, *14*, 2233. [CrossRef]
10. Sun, Z.; Baddour, N. Waveform Selection Based on Discrete Prolate Spheroidal Sequences for Near-Optimal SNRs for Photoacoustic Applications. *Photonics* **2023**, *10*, 1031. [CrossRef]
11. Fu, Q.; Zhu, R.; Song, J.; Yang, H.; Chen, X. Photoacoustic Imaging: Contrast Agents and Their Biomedical Applications. *Adv. Mater.* **2019**, *31*, 1805875. [CrossRef] [PubMed]
12. Upputuri, P.K.; Pramanik, M. Recent Advances in Photoacoustic Contrast Agents for in Vivo Imaging. *WIREs Nanomed. Nanobiotechnol.* **2020**, *12*, e1618. [CrossRef] [PubMed]
13. Jangjoo, A.; Lashkari, B.; Sivagurunathan, K.; Mandelis, A.; Baezzat, M.R. Truncated Correlation Photoacoustic Coherence Tomography: An Axial Resolution Enhancement Imaging Modality. *Photoacoustics* **2021**, *23*, 100277. [CrossRef] [PubMed]
14. Sun, Z.; Baddour, N.; Mandelis, A. Waveform Engineering Analysis of Photoacoustic Radar Chirp Parameters for Spatial Resolution and SNR Optimization. *Photoacoustics* **2019**, *14*, 49–66. [CrossRef] [PubMed]
15. Chen, Y.-S.; Yoon, S.J.; Frey, W.; Dockery, M.; Emelianov, S. Dynamic Contrast-Enhanced Photoacoustic Imaging Using Photothermal Stimuli-Responsive Composite Nanomodulators. *Nat. Commun.* **2017**, *8*, 15782. [CrossRef]
16. Burgholzer, P.; Mayr, G.; Thummerer, G.; Haltmeier, M. Linking Information Theory and Thermodynamics to Spatial Resolution in Photothermal and Photoacoustic Imaging. *J. Appl. Phys.* **2020**, *128*, 171102. [CrossRef]
17. Zhou, M.; Xia, H.; Zhong, H.; Zhang, J.; Gao, F. A Noise Reduction Method for Photoacoustic Imaging In Vivo Based on EMD and Conditional Mutual Information. *IEEE Photonics J.* **2019**, *11*, 1–10. [CrossRef]
18. Bell, M.R. Information Theory and Radar Waveform Design. *IEEE Trans. Inf. Theory* **1993**, *39*, 1578–1597. [CrossRef]
19. Liu, Y.; Liao, G.; Xu, J.; Yang, Z.; Zhang, Y. Adaptive OFDM Integrated Radar and Communications Waveform Design Based on Information Theory. *IEEE Commun. Lett.* **2017**, *21*, 2174–2177. [CrossRef]
20. Woodward, P.M. *Probability and Information Theory: With Applications to Radar*; Pergamon Science Series; Electronics and Waves, a Series of Monographs; McGraw-Hill: New York, NY, USA, 1955.
21. Yang, Y.; Blum, R.S. MIMO Radar Waveform Design Based on Mutual Information and Minimum Mean-Square Error Estimation. *IEEE Trans. Aerosp. Electron. Syst.* **2007**, *43*, 330–343. [CrossRef]
22. Wu, Z.; Li, Y.; Chang, T. Discrete Signal Reconstruction from Its Spectral Magnitude and Some Samples. In Proceedings of the ICASSP '86: IEEE International Conference on Acoustics, Speech, and Signal Processing, Tokyo, Japan, 7–11 April 1986; Institute of Electrical and Electronics Engineers: Tokyo, Japan, 1986; Volume 11, pp. 1669–1672.
23. Lashkari, B.; Mandelis, A. Linear Frequency Modulation Photoacoustic Radar: Optimal Bandwidth and Signal-to-Noise Ratio for Frequency-Domain Imaging of Turbid Media. *J. Acoust. Soc. Am.* **2011**, *130*, 1313–1324. [CrossRef]

24. Diebold, G.J.; Khan, M.I.; Park, S.M. Photoacoustic "Signatures" of Particulate Matter: Optical Production of Acoustic Monopole Radiation. *Science* **1990**, *250*, 101–105. [CrossRef]
25. Wang, L.V. Tutorial on Photoacoustic Microscopy and Computed Tomography. *IEEE J. Sel. Top. Quantum Electron.* **2008**, *14*, 171–179. [CrossRef]
26. Baddour, N. Multidimensional Wave Field Signal Theory: Mathematical Foundations. *AIP Adv.* **2011**, *1*, 022120. [CrossRef]
27. Hysi, E.; Fadhel, M.N.; Moore, M.J.; Zalev, J.; Strohm, E.M.; Kolios, M.C. Insights into Photoacoustic Speckle and Applications in Tumor Characterization. *Photoacoustics* **2019**, *14*, 37–48. [CrossRef]
28. Photoacoustic Tomography. In *Biomedical Optics*; John Wiley & Sons, Ltd.: Hoboken, NJ, USA, 2009; pp. 283–321. ISBN 978-0-470-17701-3.
29. Guo, Z.; Li, L.; Wang, L.V. On the Speckle-Free Nature of Photoacoustic Tomography. *Med. Phys.* **2009**, *36*, 4084–4088. [CrossRef]
30. Boykov, I.V.; Pivkina, A.A. On an Approximate Method for Recovering a Function from Its Autocorrelation Function. *Tech. Phys.* **2022**, *67*, 749–754. [CrossRef]
31. Boykov, I.V.; Pivkina, A.A. Signals Recovery by the Amplitude of the Spectrum. *Meas. Tech.* **2023**, *65*, 750–762. [CrossRef]
32. Yagle, A.E. Phase Retrieval from Fourier Magnitude and Several Initial Time Samples Using Newton's Formulae. *IEEE Trans. Signal Process.* **1998**, *46*, 2054–2056. [CrossRef]
33. Winkler, A.M.; Maslov, K.; Wang, L.V. Noise-Equivalent Sensitivity of Photoacoustics. *J. Biomed. Opt.* **2013**, *18*, 097003. [CrossRef]
34. Telenkov, S.; Mandelis, A. Signal-to-Noise Analysis of Biomedical Photoacoustic Measurements in Time and Frequency Domains. *Rev. Sci. Instrum.* **2010**, *81*, 124901. [CrossRef] [PubMed]
35. Winburn, D.C. *American National Standards Institute's ANSI Z136.1 "Safe Use of Lasers." In Practical Laser Safety*; CRC Press: Boca Raton, FL, USA, 1990; ISBN 978-0-203-74238-9.
36. Savateeva, E.V.; Karabutov, A.A.; Solomatin, S.V.; Oraevsky, A.A. Optical Properties of Blood at Various Levels of Oxygenation Studied by Time-Resolved Detection of Laser-Induced Pressure Profiles. In Proceedings of the Biomedical Optoacoustics III, San Jose, CA, USA, 10 June 2002; SPIE: Bellingham, WA, USA, 2002; Volume 4618, pp. 63–75.
37. Yao, D.-K.; Zhang, C.; Maslov, K.; Wang, L. Photoacoustic Measurement of the Gruneisen Parameter of Tissue. *J. Biomed. Opt.* **2014**, *19*, 17007. [CrossRef] [PubMed]
38. Yao, J.; Wang, L.V. Photoacoustic Tomography: Fundamentals, Advances and Prospects. *Contrast Media Mol. Imaging* **2011**, *6*, 332–345. [CrossRef] [PubMed]